

A Three-Dimensional Transport Model for Determining Absorbed Fractions of Energy for Electrons Within Trabecular Bone

Lionel G. Bouchet, Derek W. Jokisch and Wesley E. Bolch

Department of Nuclear and Radiological Engineering, University of Florida, Gainesville, Florida

Bone marrow is generally the dose-limiting organ of concern in radioimmunotherapy and in radionuclide palliation of bone pain. However, skeletal dosimetry is complicated by the intricate nature of its microstructure, which can vary greatly throughout skeletal regions. In this article, a new three-dimensional electron transport model for trabecular bone is introduced, based on Monte Carlo transport and on bone microstructure information for several trabecular bone sites.

Methods: Marrow cavity and trabecular chord length distributions originally published by Spiers et al. were randomly sampled to create alternating regions of bone, endosteum and marrow during the three-dimensional transport of single electrons. For the marrow spaces, explicit consideration of the site-specific elemental composition was made in the transport calculations based on the percentage of active and inactive marrow in each region. The electron transport was performed with the EGS4 electron transport code and the parameter reduced electron-step transport algorithm. Electron absorbed fractions of energy were tabulated for seven adult trabecular bone sites, considering three source and target regions: the trabecular marrow space (TMS), the trabecular bone endosteum (TBE) and the trabecular bone volume (TBV). **Results:** For all source-target combinations, the absorbed fraction was seen to vary widely within the skeleton. These variations can be directly attributed to the differences in the trabecular microstructure of the different skeletal regions. For many source-target combinations, substantial energy dependence was seen in the calculated absorbed fraction, a factor not considered in values recommended by the International Commission on Radiological Protection (ICRP). A one-dimensional model of electron transport in trabecular bone, based on range-energy relationships, was also developed to verify the three-dimensional transport model and to evaluate differences between the two modeling approaches. Differences of ~10%–15% were seen, particularly at low electron energies. In the case of a TBV source and a TMS target (or vice versa), differences >50% were seen in the absorbed fraction. **Conclusion:** The three-dimensional model of electron transport in trabecular bone allows improved estimates of skeletal absorbed fractions. The model highlights both the regional and the energy dependency of the absorbed fraction not previously considered in the ICRP model.

Key Words: dosimetry; trabecular bone; absorbed fractions; Monte Carlo transport; EGS4

J Nucl Med 1999; 40:1947–1966

Received Nov. 12, 1998; revision accepted Jun. 21, 1999.

For correspondence or reprints contact: Wesley E. Bolch, PhD, Department of Nuclear and Radiological Engineering, University of Florida, Gainesville, FL 32611-8300.

In radioimmunotherapy and in radionuclide bone pain palliation, the skeletal system, more precisely the bone marrow, is the dose-limiting organ (1–3). Radiosensitive cells in the human skeletal system have been identified as (a) hematopoietic cells present in bone marrow, (b) endosteal cells lying close to bone surfaces and (c) epithelial cells close to bone surfaces in the air sinuses of the skull (4). Unfortunately, because of the complex microstructure of the skeleton, it has been difficult to calculate accurately the dose deposited to these sensitive tissues.

The human skeletal system is formed of two different structures, as shown in Figure 1. The first is a hard, dense structure called cortical or compact bone, found in the shafts of the long bones and in the outer cortex of all bones. The dominant microstructure of the cortical bone is the osteon, which is formed of a central Haversian canal lined with a layer of endosteum and surrounded by bone lamellae. The dosimetrically important region in the cortical bone consists of osteogenic cells within the endosteal layer. A new dosimetric model of the cortical bone has been presented by Bouchet and Bolch (6).

The second structure of the skeletal system is a porous, spongy structure called the trabecular or cancellous bone. Trabecular bone is found in the interior of the flat bones and at the ends of the long bones. It is formed of a complex network of bone trabeculae and tissue cavities. Each cavity is lined by a layer of osteogenic cells, called the endosteum, and is filled with marrow that can be either hematopoietically active (red marrow) or inactive (yellow marrow). The dosimetrically important tissues in the trabecular bone are the hematopoietic stem and precursor cells in the marrow cavities and the osteogenic cells on the surfaces of the bone trabeculae.

A three-dimensional model of electron transport in trabecular bone is presented here. This model uses the chord length distribution measurements through trabecular cavities and bone trabeculae obtained by Beddoe (7), Beddoe et al. (8) and Darley (9), and randomly creates the trabecular bone regions as the electron is transported. This model is to be considered a transport model and not a fixed geometric model. Indeed, this process simulates the random mixture of

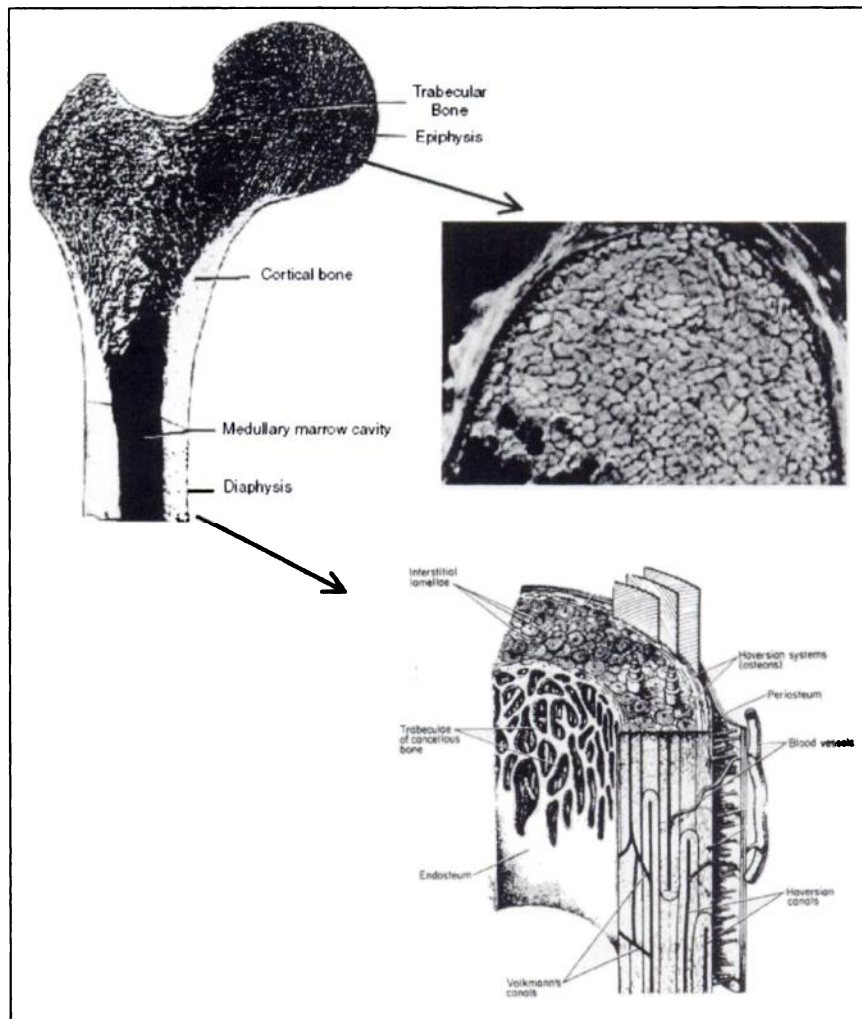


FIGURE 1. Diagram of upper half of femur showing trabecular bone regions in femur head (MR image) and neck and cortical bone regions in diaphysis (lower diagram) (adapted from [5]).

marrow cavities and bone trabeculae seen by a particle traversing trabecular bone, but the model does not recreate the true three-dimensional appearance of trabecular bone. Subsequently, absorbed fractions of energy are calculated for monoenergetic electron sources using the EGS4/parameter reduced electron-step transport algorithm (PRESTA) Monte Carlo transport code (10–12). A comparison of dosimetric results obtained via one-dimensional transport and three-dimensional transport is also presented.

PREVIOUS DOSIMETRIC MODELS OF TRABECULAR BONE

Studies at University of Leeds

The foundation of trabecular bone dosimetry was established with the work of Spiers and his research team at the University of Leeds between 1949 and 1981 (7,9,13–18). From this research group, three major dissertations on bone dosimetry are of note: Beddoe (7), Darley (9) and Whitwell (17). Spiers determined through this research that the microstructure of trabecular bone could not be described using simple geometric shapes. Instead, he used frequency distributions of linear path lengths through trabeculae and

marrow cavities as a quantitative description of the three-dimensional structure of this region of the skeleton (19). For this purpose, Beddoe (7), Beddoe et al. (8) and Darley (9) designed an optical bone scanner capable of automatically measuring bone and cavity space chord length distributions of thin sections of human trabecular bone. Assuming a direction of alignment of the cavities, they derived corresponding omnidirectional chord length distributions. Figure 2 gives the probability density function of a given chord length for trabecular cavities and bone trabeculae, respectively, for two bone sites: the parietal bone and the lumbar vertebra. A total of seven bone sites was measured, including the cervical vertebra, the lumbar vertebra, the femur head, the femur neck, the iliac crest, the parietal bone and the rib (Table 1). Whitwell (17) and Whitwell and Spiers (18) used the experimentally measured omnidirectional chord length distributions along with range-energy relationships to calculate dose conversion factors for seven radionuclides of interest in health physics (^{14}C , ^{18}F , ^{22}Na , ^{32}P , ^{45}Ca , ^{90}Sr and ^{90}Y). In that study, only bone- and surface-seeking radionuclides were considered, and only the marrow and endosteum were chosen as target regions.

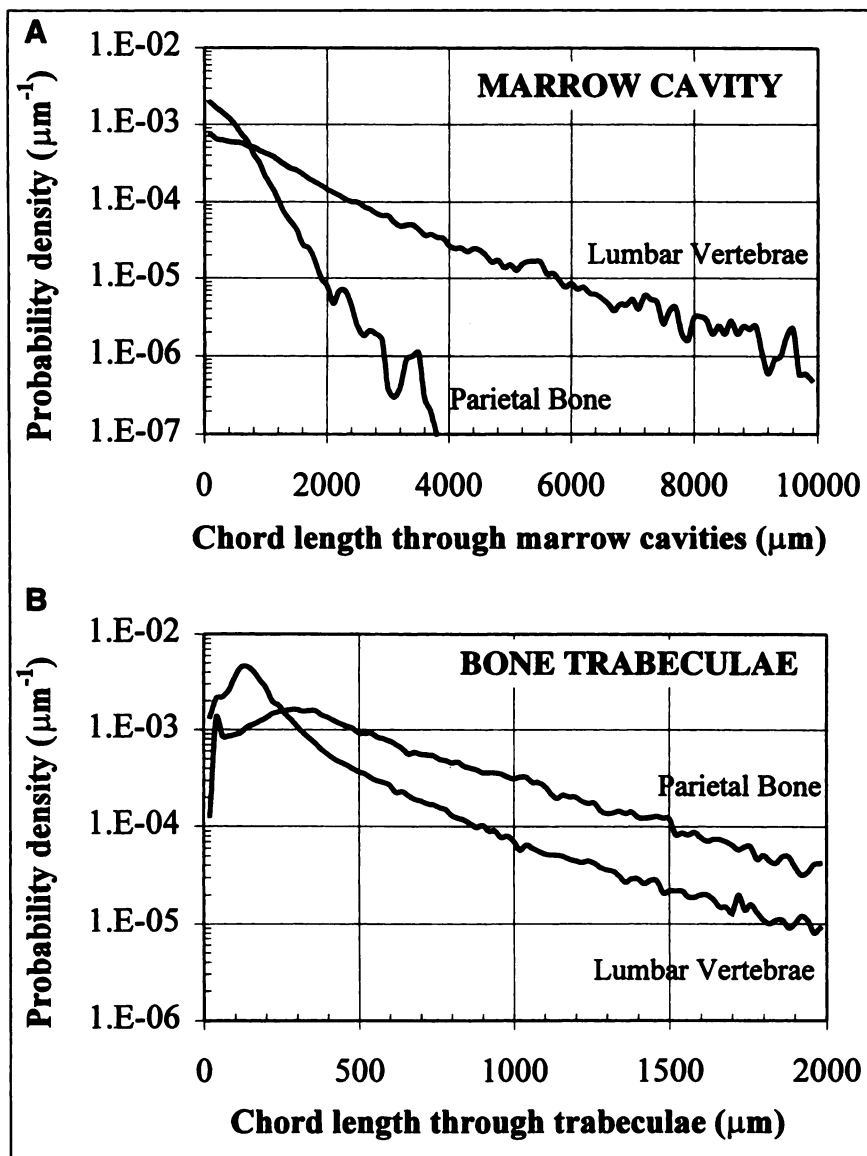


FIGURE 2. Chord length distributions for parietal bone and for lumbar vertebra through marrow cavities (A) and bone trabeculae (B).

TABLE 1
Mean Trabeculae and Cavity Chord Lengths for Seven Trabecular Bone Sites in 44-Year-Old Man

Bone site	Mean trabeculae chord length (μm)	Mean marrow cavity chord length (μm)	Ratio of trabecular and marrow mean chord lengths
Parietal bone	511	389	1.315
Cervical vertebra	279	910	0.307
Lumbar vertebra	246	1234	0.199
Rib	266	1706	0.156
Iliac crest	242	904	0.268
Femur head	232	1157	0.200
Femur neck	314	1655	0.190

Data from Beddoe (7), Beddoe et al. (8) and Darley (9).

Medical Internal Radiation Dose Pamphlet No. 11

The work of Whitwell focused on radionuclides of interest for radiation protection, and, therefore, nuclear medicine dosimetry was not of primary importance. In 1974, Snyder et al. (20) converted the skeletal-averaged dose conversion factors for given radionuclides to monoenergetic specific absorbed fractions using the average beta-particle energy of each radionuclide considered by Whitwell. Using these specific absorbed fractions, trabecular bone S values were tabulated as part of Medical Internal Radiation Dose (MIRD) Pamphlet No. 11 (21). Whitwell had not considered explicitly the marrow as a source region, a factor generally not relevant in health physics. Consequently, Snyder used conservation of energy and the uniform isotropic model (reciprocity relationship) to obtain S values for the marrow as a source. However, the uniform isotropic model is only valid in homogeneous media (22,23). Despite these limita-

tions, S values were tabulated as part of MIRD Pamphlet No. 11 (21) using these assumptions.

International Commission on Radiological Protection Publication 30

In 1979, the International Commission on Radiological Protection (ICRP) recommended in Publication 30 (24) absorbed fractions of energy for beta particles for use in radiation protection of skeletal tissues. For beta particles originating in the bone volume, a single value of absorbed fraction was recommended. For beta particles originating on the bone surface, one absorbed fraction for low-energy beta particles (average beta energy < 0.2 MeV) and one for high-energy beta particles (average beta energy > 0.2 MeV) were recommended. Table 2 summarizes the ICRP-recommended skeletal absorbed fractions of energy. These absorbed fraction values are based on the dose conversion factors from Whitwell (17) and Whitwell and Spiers (18). Subsequently, these relatively energy-independent absorbed fractions of energy were implemented in the MIRDOSE2 program for use in nuclear medicine dosimetry (25). In the MIRDOSE2 program, the self-absorbed fraction to the marrow was assumed to be unity, as suggested in Part 3 of ICRP Publication 30 (24).

Eckerman Model

In 1985, Eckerman (26) presented new absorbed fraction calculations based on the chord length distributions measured by Beddoe (7), Beddoe et al. (8) and Darley (9). Using Whitwell's approach of sampling of chord length distributions and using an electron range-energy relationship, he derived absorbed fractions of energy for monoener-

getic electrons for seven trabecular bone sites. These calculations were intended primarily to be used in radiation protection for photon sources in the Oak Ridge National Laboratory mathematic phantoms (27), through the construction of photon fluence-to-dose conversion factors. In 1994, S values derived from these calculations were implemented in the MIRDOSE 3 program to be used in nuclear medicine dosimetry (25).

Samaratunga Bone Model

In 1995, Samaratunga et al. (28) developed a more elaborate trabecular bone dosimetric model designed specifically to calculate the dose to skeletal metastases from the surface-seeker ¹⁸⁶Re. They first measured chord length distributions of cavities and bone trabeculae on 25 samples from skeletal metastases. Bone trabeculae were then represented by ellipsoids located in an infinite marrow-tissue medium. Finally, the transport of electrons was simulated in a three-dimensional geometry using the Monte Carlo electron transport code EGS4. Although the procedure was sophisticated, it was intended for transport of electrons in trabecular bone metastases and is therefore not applicable to Reference Man tabulations.

MATERIALS AND METHODS

Although elegant in design, the one-dimensional computational models of Whitwell and Spiers (18) and Eckerman (26) are based on the assumptions that (a) particle trajectories are linear through both the bone matrix of the trabeculae and the marrow cavities, such that a given chord length explicitly represents the particle path (no angular scatter); (b) energy loss within these structures can be treated under the continuous slowing-down approximation; and (c) the transport of energy by delta rays and bremsstrahlung photons can be ignored. The computational model presented here attempts to account for each of these mechanisms by performing a three-dimensional transport of electrons using the EGS4/PRESTA radiation transport code (10,11). The base input data for the model are the same chord length distributions measured by the research group of Spiers (7-9,17). These chord length distributions represent the most complete quantitative information assembled to date on the microstructure of adult trabecular bone.

Transport Model

The chord length distributions measured by the research group of Spiers (7-9,17) represent the distribution of distances that one would see if crossing trabecular bone in many directions. If one considers an electron traveling in trabecular bone, the chord length distributions can be thought of as the distribution of distances between entry and exit points of a given trabecular bone region. This concept is illustrated in Figure 3, where an electron and one of its delta rays are shown. In Figure 3, distances d_T and d_{MC} denote distances between entry and exit points of the bone trabeculae (T) and the marrow cavities (MC), respectively. (In the sample preparation procedures of Spiers et al., all marrow tissues including endosteum were removed before optical scanning. Consequently, we make a distinction here between [a] the marrow cavity [total volume between bone trabeculae inclusive of the endosteal layers] and [b] the marrow space [volume interior to both the bone trabeculae and endosteum].) The chord length distributions can therefore be used to limit the travel of an electron in a given

TABLE 2

Recommended Skeletal Absorbed Fractions of Energy for Trabecular Bone Given in ICRP Publication 30

Source	Target	ICRP 30 absorbed fraction
Red marrow	Red marrow	1.0*
	Endosteum†	0.02‡
Endosteum	Red marrow	0.5
	Endosteum	0.25 for $\bar{E}_\beta < 0.2$ MeV 0.025 for $\bar{E}_\beta \geq 0.2$ MeV
Trabeculae	Red marrow	0.35
	Endosteum	0.025

*It is only within preface to Part 3 of ICRP Publication 30 (24) that marrow sources are specifically addressed. It is here that ICRP specifies that absorbed fraction to marrow is assumed to equal 1.0 for beta particles emitted with marrow spaces of trabecular bone.

†The endosteum is referred to in ICRP Publication 30 as "bone surfaces."

‡Also in preface to Part 3 of ICRP Publication 30, Commission indicates that "dose equivalent in whole of bone surfaces is taken to be half of that in red marrow." Using reference masses of 60 g for trabecular endosteum and 1500 g for red marrow, approximate absorbed fraction for marrow sources irradiating trabecular endosteum would be 0.02.

ICRP = International Commission on Radiological Protection.

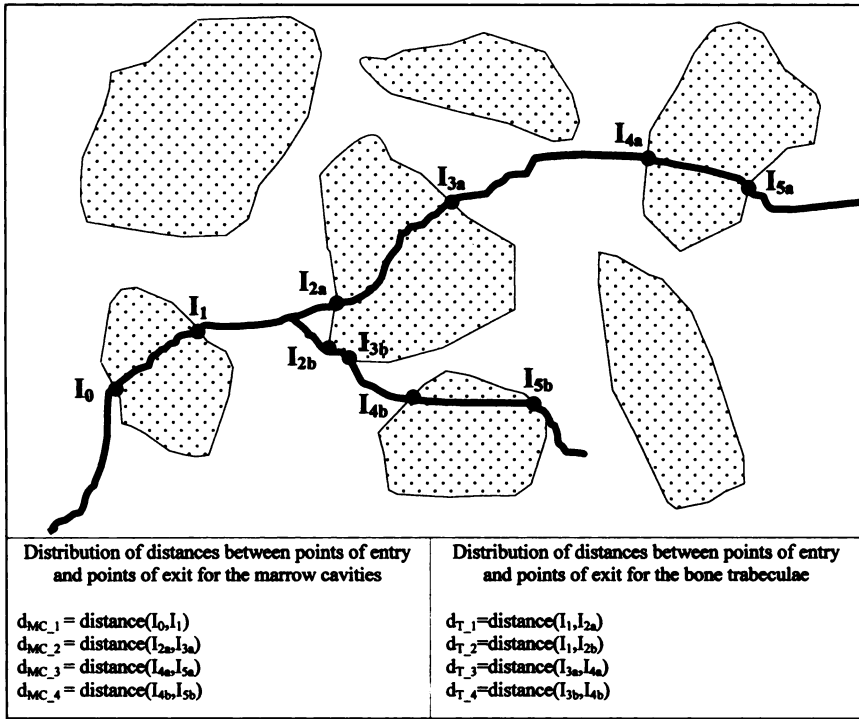


FIGURE 3. Diagram showing electron passing through region of trabecular bone. Marrow cavities are represented as textured areas. Entry and exit points of any new trabecular bone region that electron encounters along its path are shown. Distribution of distances between points for cavities and bone trabeculae represent measured chord length distributions obtained by Beddoe (7), Beddoe et al. (8) and Darley (9).

trabecular bone region by assuming the distance between the points of entry and exit of a given region to be equal to the sampled chord length for this region. By randomly sampling many chord lengths, and by considering many electrons, the average transport behavior of electrons in trabecular bone is thus realized.

Figure 4A illustrates how the transport of the electron in a given trabecular bone region (trabeculae or marrow cavity) is limited using a sampled chord length (d_T or d_{MC}). The electron first enters a trabecula or marrow cavity at point I_0 . At this point, a chord length d_T or d_{MC} is randomly selected, thus limiting the point of exit (I_1) of the electron to distance d_T or d_{MC} from I_0 . This exit point is therefore located on a sphere centered on I_0 , with radius d_T or d_{MC} . To allow for electron backscatter, the sphere is further limited by a plane at I_0 , perpendicular to the direction of travel at the point of entry. This method defines a hemisphere as the surface delimiting all possible points of exit I_1 of the electron. Thus, when entering a new region, the electron's distance of travel between two regions (straight-line distance) is limited; however, within a given region, the electron is allowed to travel in three dimensions. Consequently, one can have a total electron path length traveled in a given region greater than d_T or d_{MC} , the distance physically separating the two different trabecular bone regions.

Chord length distributions are available only for the marrow cavities and for the bone trabeculae. For the endosteum, chord length information is not available. Nevertheless, the ICRP recommends a reference thickness of 10 μm for the endosteal cells on bone surfaces (4,29,30). This reference thickness is consistent with the definition that the endosteum is composed of a single cell layer (5). Whitwell (17) further noted that 99% of the endosteal layer has a thickness ≤ 5.0 – $8.5 \mu\text{m}$. Using a 10- μm thickness of tissue to represent the endosteum, and assuming that a particle's entry direction to the endosteum is isotropic, it is possible to select randomly a chord length through this tissue region. When the particle enters the endosteum, an isotropic direction of entry is selected and a corresponding chord (d_E) through the 10- μm

endosteal layer is derived. Mathematically, one samples η , the cosine of the entry angle, uniformly between 0 and 1:

$$\eta \in [0; 1] \quad \text{and} \quad d_E = (10 \mu\text{m})/\eta. \quad \text{Eq. 1}$$

As noted earlier, this derived chord length through the endosteum was inclusive to the marrow cavity chord lengths measured by the research group of Spiers (7–9,17). Therefore, for any sampled marrow cavity chord length d_{MC} , one must select two endosteal chords d_{E1} and d_{E2} and a marrow space chord d_{MS} , so that:

$$d_{MC} = d_{E1} + d_{MS} + d_{E2}. \quad \text{Eq. 2}$$

This last equation limits the endosteal chord length, so that:

$$d_{MC} = d_{E1} + d_{E2}, \quad \text{and} \\ d_{MS} = 0, \quad \text{Eq. 3}$$

which corresponds to a chord measurement through only the near and far endosteal layers. This notion of endosteal chord lengths and marrow space chord lengths is illustrated in Figure 4B. In this figure, two marrow cavity chords are shown: one defining three chords (as in Equation 2) and the other defining two chords (as in Equation 3). In summary, for each sampled marrow cavity chord length d_{MC} , one first calculates two endosteal chords according to Equation 1, using the two random entry and exit cosine angles η_1 and η_2 . Then, if $d_{E1} + d_{E2} \geq d_{MC}$:

$$d_{E1} = d_{E2} = \frac{d_{MC}}{2}, \quad \text{and} \\ d_{MS} = 0. \quad \text{Eq. 4}$$

Otherwise, if $d_{E1} + d_{E2} \leq d_{MC}$:

$$d_{E1} = (10 \mu\text{m})/\eta_1, \\ d_{E2} = (10 \mu\text{m})/\eta_2, \quad \text{and} \\ d_{MS} = d_{MC} - (d_{E1} + d_{E2}). \quad \text{Eq. 5}$$

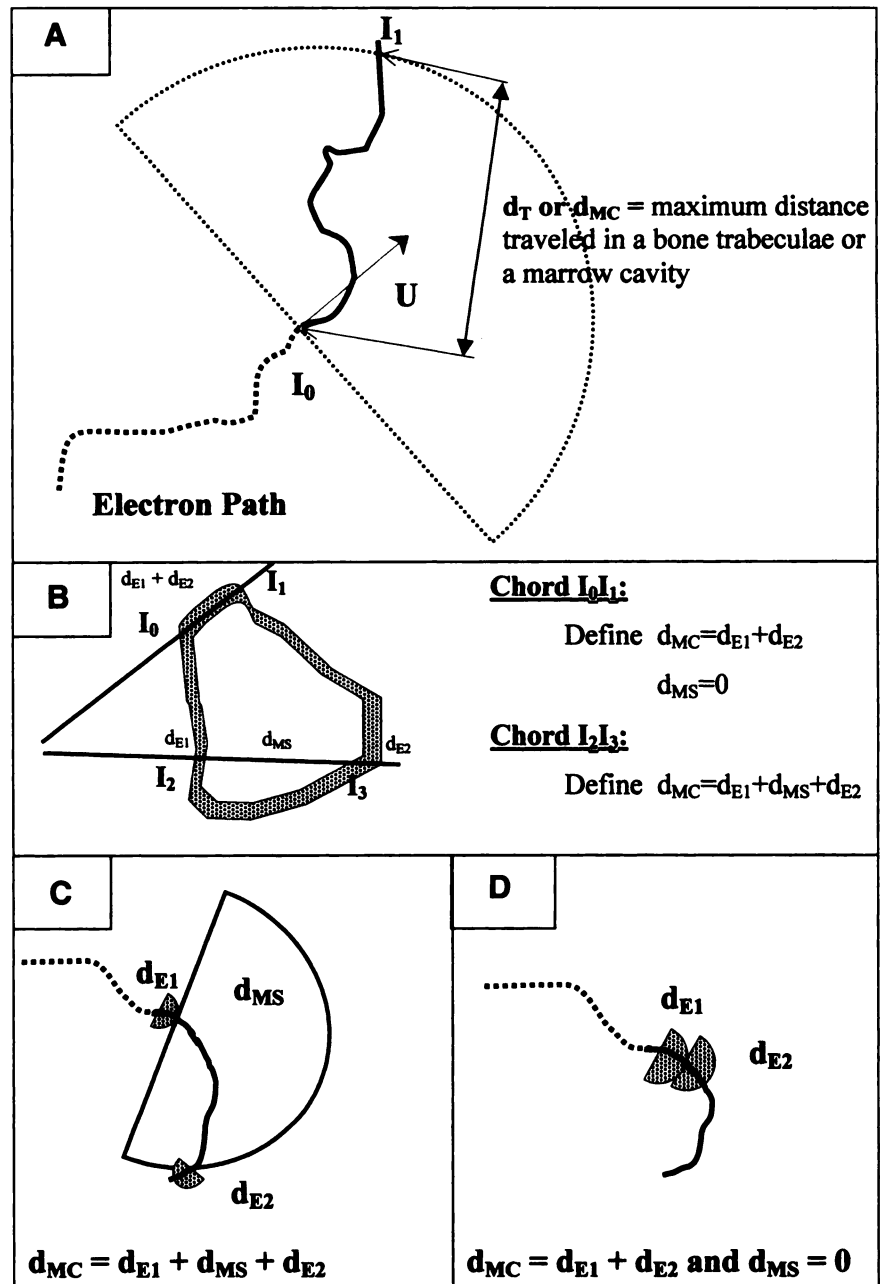


FIGURE 4. Diagram illustrating three-dimensional electron transport model. (A) How sampled chord length is used to limit electron transport by creation of hemisphere. (B) Derivation of chord through near and far endosteal layers (d_{E1} and d_{E2}) and through marrow space (d_{MS}) from marrow cavity chord length (d_{MC}). (C and D) How derived chords (d_{E1} , d_{E2} and d_{MS}) are used to limit the extent of electron transport.

Each derived chord length is then used to limit the electron transport, using a hemispheric transport region as shown in Figures 4C and D.

To initiate the transport of an electron within a given trabecular bone region, the starting region must first be considered. If a particle originates within the marrow cavity or the bone trabeculae, the distance to the nearest boundary follows a distribution different from the chord length distributions measured by the research group of Spiers (7-9,17). There are three types of distributions of chord lengths in convex bodies of interest in radiation dosimetry (31-33). The first is mean-free-path randomness, or μ -randomness, where a chord is defined by a point in space and a given direction through a convex body. The second is surface radiator randomness, or S-randomness, where a chord is defined by a point on the surface of the convex body and a given direction. The third is interior

randomness, or I-randomness, where a chord is defined by a point interior to the convex body along a given direction. To generate chord distributions, the directions and starting points are selected from independent uniform distributions. Figure 5 summarizes the three different chord length distributions. For our purposes, the I-random chord distribution is of interest when the particle originates within a given region. The measurements of chord length distributions in trabecular bone performed by the research group of Spiers (7-9,17) were made under the conditions of μ -randomness. To derive an I-random chord distribution from a μ -random chord distribution, the following relationship can be used:

$$f_I(d) = \frac{d}{\langle d \rangle_\mu} f_\mu(d), \quad \text{Eq. 6}$$

where $f_I(d)$ and $f_\mu(d)$ are the probability density functions for chord

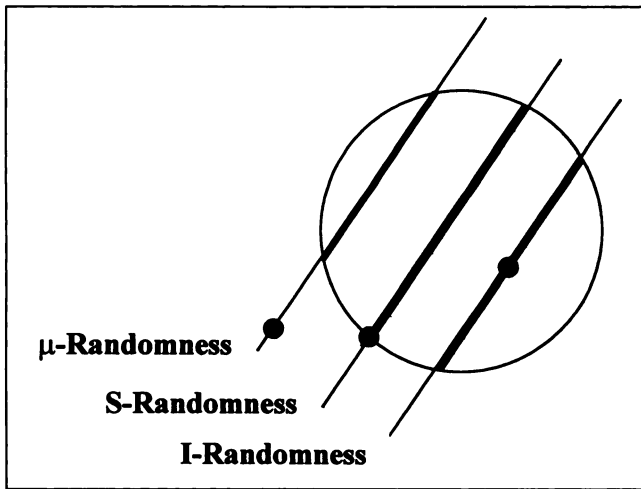


FIGURE 5. Illustration of three different types of chords within convex body of interest in radiation dosimetry: μ -randomness, S-randomness and I-randomness.

lengths under I- and μ -randomness, respectively, and $(d)_\mu$ is the average chord length under μ -randomness (31). Thus, using this derived I-random chord distribution, an interior chord length d_i can be obtained for both trabecular cavities and bone trabeculae. After choosing an interior chord d_i , a starting internal distance d_0 between 0 and d_i is randomly selected. This selected distance thus limits the distance traveled by the electron in the initial source

region. The electron enters a new region created as described using its direction of travel and the μ -random chord length distribution. Figure 6 shows the geometry that is presented to the electron to simulate its transport in trabecular bone. A backscattered electron and the creation of a delta ray are also shown in Figure 6. This process is continued until the kinetic energy of the followed particle decreases below a defined limit.

This method of determination of the initial region for the transport of electrons in trabecular bone can be applied for bone volume sources, where the bone trabeculae is the starting region, and for marrow sources, where the marrow space is the starting region. For surface sources, where the endosteum is the source region, chord length distributions are not available; only the reference thickness of the endosteum is available. In this case, the starting particle is randomly selected between two planes separated by an average thickness of 10 μm , and its initial direction is chosen randomly. The only concern here could be the curvature of the surfaces of the endosteum, which is taken as infinite in the case of two parallel planes. However, because of the small thickness of the two planes, this inexact modeling of the true bone endosteum curvature is of concern only for very-low-energy electrons. These short-range electrons expend a greater fraction of their initial energy within the source endosteal layer, and thus their values of absorbed fraction will vary more rapidly with increasing surface curvature than those of high-energy, longer-range endosteal source electrons. Once the electron escapes the $Z = 10\text{-}\mu\text{m}$ plane, a new trabeculae bone region hemisphere is randomly selected. If it escapes the $Z = 0\text{-}\mu\text{m}$ plane, a new marrow cavity region is selected. Figure 7 shows a

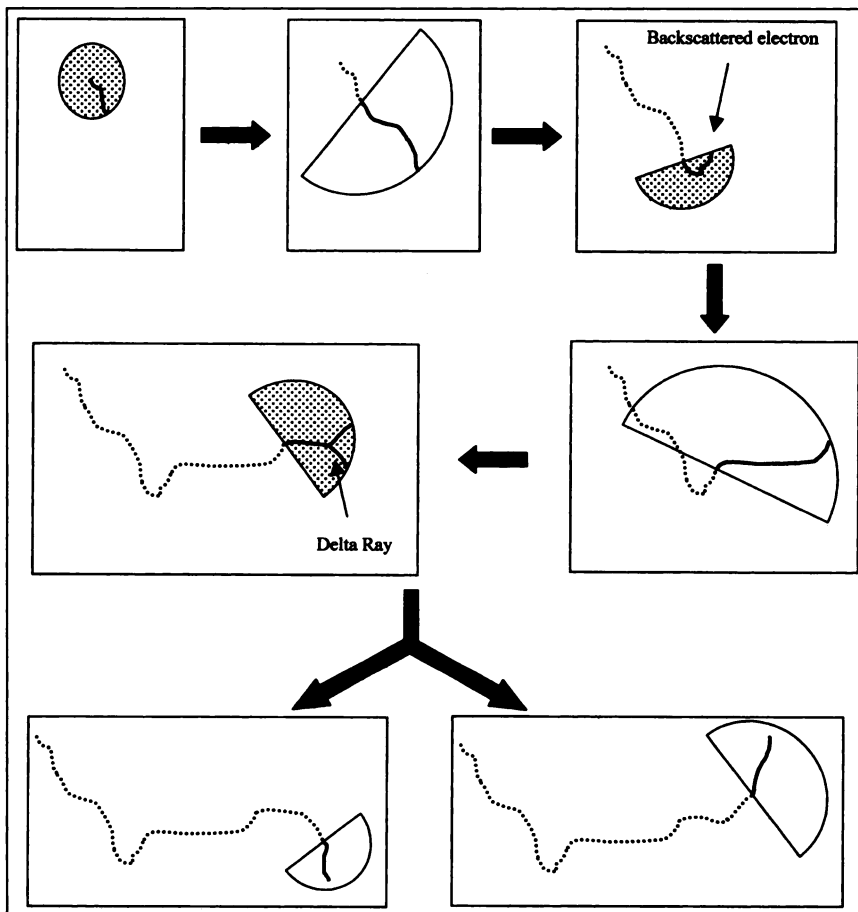


FIGURE 6. Model of electron transport in trabecular bone. Textured areas are bone trabeculae regions; white areas are marrow space regions. Endosteal hemispheres are not shown because of their relatively small size. Backscattered electron and delta ray are represented.

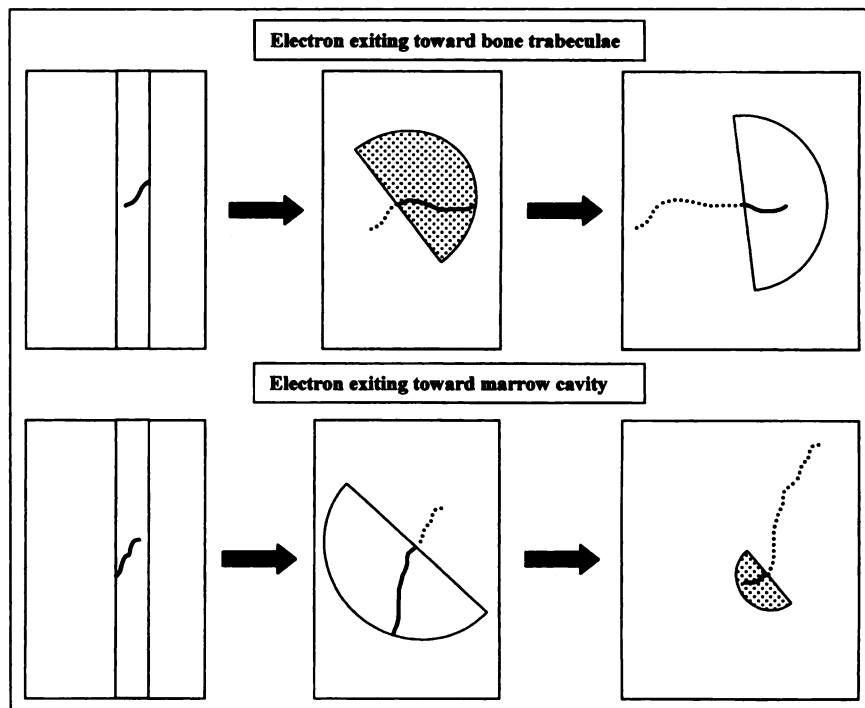


FIGURE 7. Model of electron transport in trabecular bone where endosteum is source region. Textured areas are bone trabeculae regions; white areas are marrow cavity regions. Top panel series shows electron exiting endosteal layer toward bone trabeculae ($Z = 10 \mu\text{m}$). Bottom panel series shows electron exiting endosteal layer bordering marrow space ($Z = 0 \mu\text{m}$). Subsequent endosteal hemispheres are not shown because of their small relative size.

diagram of the geometry presented to the electron in the case of an endosteum electron source within the trabecular bone.

The electron transport model so constructed represents a logical extension of the one-dimensional electron transport models of Whitwell (17) and Whitwell and Spiers (18) and of Eckerman (26). It allows the electron to travel in any direction and simulates the correct distribution of chord lengths that would be seen by an electron traveling in trabecular bone. Furthermore, the model can be implemented within a Monte Carlo electron transport code, thus allowing electron backscatter, bremsstrahlung photons and delta rays to be simulated. As with previous models based on the University of Leeds data, the chord length distributions for the trabeculae and marrow cavities are sampled as independent distributions. Although it is conceivable that this is not the case, particularly for bone sites with trabeculae aligned in a given load direction, the format of the Leeds data does not permit the construction of joint probability distributions for marrow and trabeculae chord lengths. Such data, however, may be readily compiled in future studies involving three-dimensional microimaging of trabecular bone specimens.

Consideration of Percent Active Marrow

An additional feature of the present model is the consideration of marrow space cellularity within different skeletal regions. The cellularity factor (CF) is defined as the fractional mass of marrow space occupied by active (red) marrow, the remainder being composed of inactive (yellow) marrow (34). For example, for trabecular bone site j , the CF can be calculated using the following equation:

$$CF_j = \frac{m_{\text{Red},j}}{m_{\text{Yellow},j} + m_{\text{Red},j}}, \quad \text{Eq. 7}$$

where $m_{\text{Red},j}$ and $m_{\text{Yellow},j}$ are the mass of red and yellow marrow in trabecular bone site j , respectively. At birth, 100% of all marrow is active. As one ages, marrow spaces within the appendicular

skeleton, and to some extent the axial skeleton, accumulate adipose tissue, thus transitioning to yellow marrow. Standard values of age-specific CFs were published in ICRP Publication 70 (5), a revision to the skeletal chapter of the Reference Man report (29). For an adult of age 40 y, the ICRP Publication assigns a CF of 0.7 for the vertebrae (e.g., cervical and lumbar vertebrae) and the ribs, 0.48 for the iliac crest and 0.38 for the parietal bone. Because a CF for the femur head and neck was not explicitly tabulated, the CF for these sites was assumed to be the same as that for the iliac crest (only the CF factor for the upper half of the femur is tabulated, and thus this value additionally reflects the marrow composition within the proximal half of the femoral shaft).

The elemental composition and density of pure red and yellow marrow have been defined in the International Commission on Radiation Units and Measurements (ICRU) Report 46 (35) and are reproduced in the first three columns of Table 3. Given these data and the four defined values of marrow cellularity, one may determine unique elemental compositions and mass densities for the marrow space within bone group i as:

$$\rho_{i,MS} = CF_i \times \rho_{\text{RM}} + (1 - CF_i) \times \rho_{\text{YM}}, \quad \text{and} \quad \text{Eq. 8}$$

$$(\% \text{mass}_i)_{MS}$$

$$= CF_i \times (\% \text{mass}_i)_{\text{RM}} + (1 - CF_i) \times (\% \text{mass}_i)_{\text{YM}}. \quad \text{Eq. 9}$$

These data are given in columns 4–6 of Table 3. Finally, the endosteal layers within the model are assigned an elemental composition defined in ICRU Report 44 (36) for the average adult male soft tissue. The composition of the trabecular regions was taken as that defined in ICRU Report 46 for adult cortical bone (35).

Transport Parameters

The EGS4 Monte Carlo transport code (11,12) and the PRESTA algorithm were used for all simulations of electron transport. The electron cutoff for kinetic energy was 1 keV for initial kinetic

TABLE 3

Elemental Composition of Regions Within Transport Model (Percentage by Mass) Derived from ICRU Reports 44 and 46*

Element	Red marrow	Yellow marrow	Medium 1†	Medium 2‡	Medium 3§	Endosteum	Trabeculae
H	10.5	11.5	10.8	11.02	11.12	10.5	3.4
C	41.4	64.4	48.3	53.36	55.66	25.6	15.5
N	3.4	0.7	2.59	2.00	1.73	2.7	4.2
O	43.9	23.1	37.66	33.08	31.00	60.2	43.5
Na	—	0.1	0.03	0.052	0.062	0.1	0.1
Mg	—	—	—	—	—	—	0.2
P	0.1	—	0.07	0.048	0.038	0.2	10.3
S	0.2	0.1	0.17	0.148	0.138	0.3	0.3
Cl	0.2	0.1	0.17	0.148	0.138	0.2	—
K	0.2	—	0.14	0.096	0.076	0.2	—
Ca	—	—	—	—	—	—	22.5
Fe	0.1	—	0.07	0.048	0.038	—	—
Mass density (g/cm ³)	1.030	0.980	1.015	1.004	0.999	1.030	1.920

*ICRU Report 44 (36); ICRU Report 46 (35).

†Medium 1 includes cervical vertebra, lumbar vertebra and rib for which cellularity factor (CF) = 0.7.

‡Medium 2 includes iliac crest and femur head and neck for which CF = 0.48.

§Medium 3 includes parietal bone for which CF = 0.38.

ICRU = International Commission on Radiological Units.

electron energies <50 keV and 10 keV for initial kinetic electron energies >50 keV. The cutoff energy for photons (PCUT and PE) was 1 keV. The maximum percent energy loss per step associated with continuous slowing down (ESTEPE) was chosen as 2%. Bremsstrahlung photons were followed up to a distance not to exceed 5 cm from the initial source point. A total of 100,000 histories were simulated per particle energy (10 runs of 10,000 histories). An average absorbed fraction and a corresponding SD were then derived for all target regions.

RESULTS AND DISCUSSION

Electron absorbed fractions of energy are calculated for the seven trabecular bone sites measured by Beddoe (7), Beddoe et al. (8) and Darley (9). Three sources and three target regions are considered: trabecular bone volume (TBV), trabecular marrow space (TMS) and trabecular bone endosteum (TBE). Twelve energies are considered between 10 keV and 4 MeV. Results are given in the Appendix in Table 1A for the TMS as a source, Table 2A for the TBE as a source and Table 3A for the TBV as a source. The calculated coefficients of variation (CVs) are less than ~0.5% when the source and the target region are equal. When the source and target are different, the CVs are less than ~5%. An exception is at very low energies (10 keV and 15 keV) for nonadjacent source-target region combinations (TBV and TMS), where some values of the CV are as high as 50%.

Marrow Space as Radiation Target

The absorbed fraction to the marrow space for monoenergetic electron sources emitted within the marrow space is shown in Figure 8A for three of the seven skeletal sites for which chord length distributions are available. At the lowest electron energy considered (10 keV), essentially all electron energy is absorbed within the target region. At increasingly higher energies, the absorbed fraction declines from unity, as

electrons begin to penetrate the endosteal layer of the source marrow space and the adjacent trabeculae. At ~500 keV to 1 MeV, electrons are able to penetrate to the marrow spaces of adjacent cavities, thus resulting in a leveling off of the absorbed fraction with further increases in emission energy.

The influence of the regional microstructure of trabecular bone is evident in Figure 8A. The absorbed fraction to the parietal bone, with its substantially smaller marrow cavities, is shown to fall more rapidly with electron energy than in the cervical vertebra or in the rib. ICRP Publication 30 suggests an energy-independent absorbed fraction of 1.0 for this source-target region combination (24). Clearly, this assumption grossly overestimates the radiation dose to this tissue region at moderate to high electron energies.

Absorbed fractions to the marrow space for TBE sources are shown in Figure 8B. ICRP Publication 30 (24) recommends an energy-independent value of 0.5 in the assumption that only 50% of the emissions on the bone surfaces emit electrons into the marrow space where they deposit their full energy. In the current model, electrons representing “surface seekers” are more properly emitted within the trabecular endosteum volume, where they must first exit the 10-µm layer before reaching the marrow space. Thus, the absorbed fraction starts close to zero at low energies and rises rapidly as a greater fraction of the initial electron energy is deposited within the first marrow cavity. At higher energies, subsequent trabeculae must be crossed before any additional energy deposition to marrow can occur. Thus, the absorbed fraction increases less rapidly with increasing initial energy. The variation of absorbed fraction with particle energy in the parietal bone is markedly different from that within the vertebral regions because of its larger bone trabeculae and smaller marrow cavities (Table 1).

Figure 8C shows the corresponding absorbed fractions to

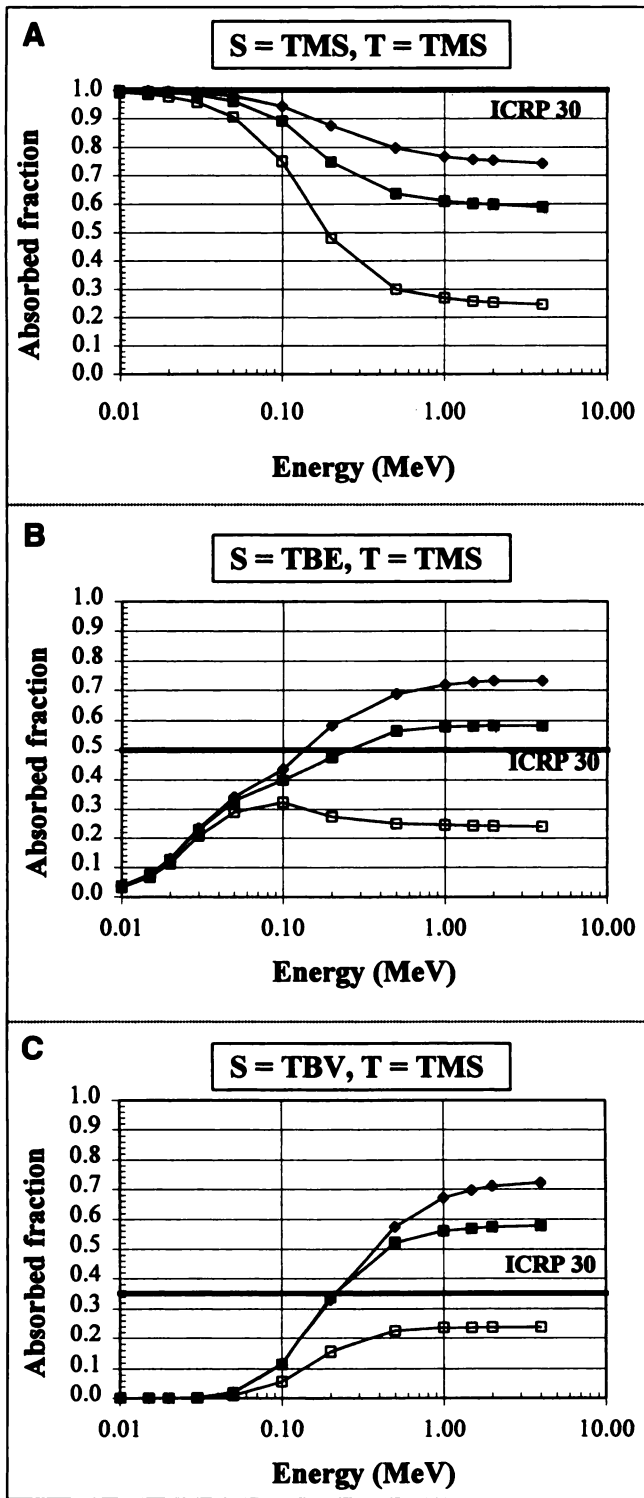


FIGURE 8. Absorbed fractions of energy to trabecular marrow space (TMS) for monoenergetic electrons for sources in TMS (A), trabecular bone endosteum (TBE) (B) and trabecular bone volume (TBV) (C). Three trabecular bone sites are shown: cervical vertebra (■), parietal bone (□) and rib (◆). International Commission on Radiological Protection (ICRP) recommended absorbed fractions are also represented (24). S = source; T = target.

the marrow space for electron sources uniformly distributed within the bone volume of the trabeculae. As with the trabecular endosteal sources, the absorbed fraction begins at zero at low energies and increases to a limiting value at high electron energies. In this case, however, electrons must pass through both the trabeculae and the endosteal layer before reaching the first marrow cavity. Consequently, the rise in absorbed fraction for bone volume sources occurs over a broader energy range than for trabecular endosteal sources. The ICRP methodology (24) assumes an energy-independent value of 0.35. This value is shown to overestimate energy absorption for low-energy electrons for all bone sites. At higher electron energies, energy absorption in the marrow space is underestimated for vertebral and rib sources and overestimated for electron sources in the skull.

For a given skeletal site, the three graphs of Figure 8 indicate a convergence of the absorbed fraction to a single value at high energies, independent of the source region (26). This limiting value corresponds to the fractional track length in the target marrow cavity for a given bone site:

$$\phi(TMS \leftarrow S) = \frac{\langle d_{MC} \rangle_{\mu} - 2\langle d_E \rangle}{\langle d_{MC} \rangle_{\mu} + \alpha \langle d_T \rangle_{\mu}}, \quad \text{Eq. 10}$$

where $\langle d_{MC} \rangle_{\mu}$ and $\langle d_T \rangle_{\mu}$ are the average chord lengths under μ -randomness for the marrow cavities (inclusive of its endosteal layers) and bone trabeculae, respectively; $\langle d_E \rangle$ is the average thickness of endosteum crossed (derived for each bone site from the transport code assuming a random entry direction of the electron into the endosteum); and α is the ratio of the range of electrons in marrow to that in bone tissue ($\alpha = \sim 1.7$ using ICRU Report 46 (35) tabulated R_{CSDA} ranges). This limit of the absorbed fraction at high energies is verified in Table 4, where the absorbed fraction for 4-MeV electrons is compared with the calculated absorbed fraction limit using Equation 10.

Trabecular Endosteum as Radiation Target

The second radiation target to consider is the endosteal tissue layer of TBE. Figure 9A shows the variation of the absorbed fraction to the TBE region for marrow sources of electrons and for the same three skeletal regions just discussed. Depending on the bone trabeculae and marrow cavity average sizes, two different variations of the absorbed fraction with energy are observed. In the case of the parietal bone, where marrow cavity sizes are small and bone trabeculae are large (Table 1), a rapid increase is first seen up to a maximum occurring at ~ 100 keV. Next, the absorbed fraction decreases slowly and levels off to a constant value for high electron energies. For the other trabecular bone regions, where the marrow cavities are much larger than the bone trabeculae, the absorbed fraction increases almost steadily in reaching a maximum value. These differences in the variation of the absorbed fractions with initial electron energy can be further investigated by data presented in Figure 10. In Figure 10, the absorbed fraction of energy is partitioned according to the various TBE regions created in

TABLE 4
Limits of Absorbed Fractions of Energy Calculated Using Average Chords Through TMS, TBE and TBV

	Average chord lengths (μm)						
	Cervical	Femur head	Femur neck	Iliac crest	Lumbar vertebra	Parietal vertebra	Rib
Trabecula	279	232	314	242	246	511	266
Marrow cavities	910	1157	1655	904	1234	389	1706
Marrow space	811	1052	1544	804	1131	309	1597
Endosteum	49	52	55	50	51	40	54
Limits of φ at high energy							
T = TMS	5.9E-01	6.8E-01	7.1E-01	6.1E-01	6.8E-01	2.5E-01	7.4E-01
T = TBE	7.1E-02	6.7E-02	5.1E-02	7.6E-02	6.2E-02	6.3E-02	5.0E-02
T = TBV	3.4E-01	2.5E-01	2.4E-01	3.1E-01	2.5E-01	6.9E-01	2.1E-01
Ratios of φ at 4 MeV to φ limit calculated for T = TMS							
S = TMS	1.00	1.00	1.00	1.00	1.00	1.00	1.00
S = TBE	0.96	0.97	0.95	0.98	0.96	0.97	0.94
S = TBV	0.96	0.96	0.95	0.96	0.95	0.98	0.94
Ratios of φ at 4 MeV to φ limit calculated for T = TBE							
S = TMS	0.99	0.99	0.99	0.99	0.99	0.98	0.99
S = TBE	0.97	1.00	0.98	0.99	0.98	0.99	0.98
S = TBV	0.97	0.98	0.98	0.98	0.98	0.98	0.98
Ratios of φ at 4 MeV to φ limit calculated for T = TBV							
S = TMS	0.98	0.98	0.97	0.98	0.98	0.97	0.97
S = TBE	0.97	0.99	0.97	0.98	0.97	0.97	0.97
S = TBV	0.99	1.00	1.02	0.99	1.01	0.99	1.03

TMS = trabecular marrow space; TBE = trabecular bone endosteum; TBV = trabecular bone volume.

Theoretical calculated averages are compared with Monte Carlo calculated averages at 4 MeV for all source (S) and target (T) combinations.

the transport code that are traversed by electrons originating in the TMS source region. Results are shown for both the parietal bone (Fig. 10A) and the cervical vertebra (Fig. 10B). For the TBE directly adjacent to the TMS source (TBE 1), the absorbed fraction of energy in the parietal bone is seen to increase more rapidly with source particle energy than in the cervical vertebra. Consequently, the unique microstructure of the parietal bone leads to a dominance of the first TBE region (adjacent) in the total value of the absorbed fraction to the trabecular endosteum. In the case of the cervical vertebra, the decrease in the absorbed fraction to the first endosteal region for source energies >200 keV is compensated by energy deposited in subsequent TBE regions, and the global absorbed fraction continues to increase with increasing source particle energy. For a TMS source and a TBE target, ICRP Publication 30 (24) recommends that:

$$\phi(\text{BS} \leftarrow \text{RM}) = \phi(\text{RM} \leftarrow \text{RM})/2, \quad \text{Eq. 11}$$

therefore giving an energy-independent absorbed fraction of 0.02 to the TBE (assuming a red marrow mass of 1500 g and a bone surface or endosteal mass of 60 g [29]). This recommendation underestimates our calculated absorbed fractions at electron energies greater than ~100 keV for the rib, at energies greater than ~50 keV for the cervical

vertebra and at energies greater than ~20 keV for the parietal bone.

For trabecular endosteal (TBE) sources, the model predicts absorbed fractions to trabecular endosteum as being relatively independent of the skeletal microstructure (Figure 9B). At 10 keV, an absorbed fraction of ~0.9 is indicated because of the small thickness of the endosteum. The value drops rapidly to reach a plateau at energies greater than about 500 keV. The methodology of ICRP Publication 30 (24) recommends a discontinuous drop in the absorbed fraction from 0.25 at energies <200 keV to a value of 0.025 at greater energies. For electron energies <50 keV and >200 keV, the ICRP 30 method underestimates the energy deposition to trabecular endosteum.

Figure 9C gives results for the absorbed fraction to the TBE for a TBV source. As in the case of TMS as the source region, there are two trends of the absorbed fraction with the electron energy, depending on the relative sizes of the bone trabeculae and marrow spaces. For the parietal bone with its larger bone trabeculae, the absorbed fraction follows a steady increase until about 1.0 MeV, where a limiting value is reached. In other skeletal regions, where smaller bone trabeculae and larger marrow cavities are found, the absorbed fraction of energy follows a trend identical to that

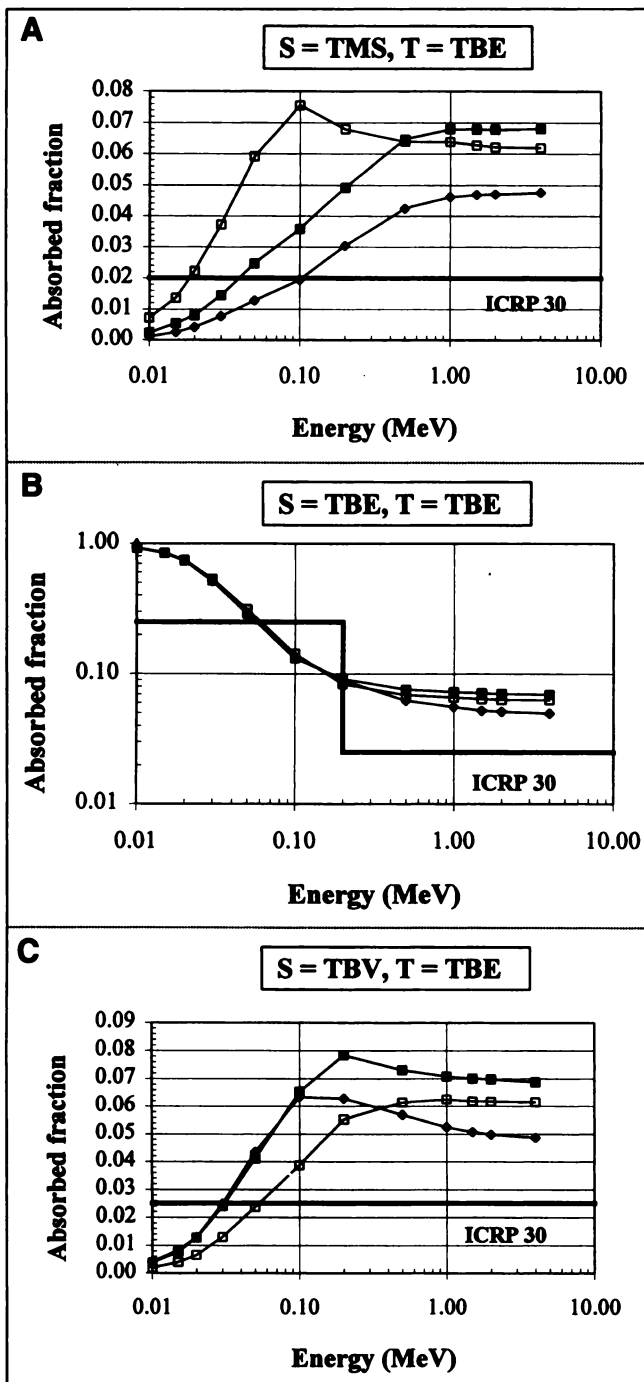


FIGURE 9. Absorbed fractions of energy to trabecular bone endosteum (TBE) for monoenergetic electrons for sources in trabecular marrow space (TMS) (A), TBE (B) and trabecular bone volume (TBV) (C). Three trabecular bone sites are shown: cervical vertebra (■), parietal bone (□) and rib (◆). International Commission on Radiological Protection (ICRP) recommended absorbed fractions are also represented in (B) and (C) (24). Graph in (B) for TBE as source (S) and target (T) region is given in logarithmic scale.

shown for the parietal bone when the marrow space was the source region (Fig. 9A). For a TBV source and a TBE target, ICRP Publication 30 (24) recommends an energy-independent absorbed fraction of 0.025 to the TBE. This recommen-

dation underestimates our calculated absorbed fractions for energies greater than ~30–50 keV.

As noted for TMS as the target region and for all three source regions, the resulting absorbed fractions at high initial energies are independent of the source region. This limiting value of the absorbed fraction corresponds to the fractional track length in the endosteal cavity for the given bone site:

$$\phi(\text{TBE} \leftarrow \text{S}) = \frac{2\langle d_E \rangle}{\langle d_{MC} \rangle_\mu + \alpha \langle d_T \rangle_\mu}, \quad \text{Eq. 12}$$

where $\langle d_{MC} \rangle_\mu$, $\langle d_T \rangle_\mu$, $\langle d_E \rangle$ and α were defined previously. The factor of 2 added in the numerator of Equation 12 takes into account the two regions of endosteum crossed when an electron enters and exits a marrow cavity. As with the TMS as target region, the limits of the absorbed fractions at large energies for each bone site are verified in Table 4.

The reference absorbed fractions recommended in ICRP Publication 30 (24) for the case of the endosteum as the target region are based on the work of Whitwell (17) and Whitwell and Spiers (18). From the graphs in Figure 9, it can be seen that these recommended absorbed fractions generally underestimate our calculated absorbed fractions. After careful analysis of Whitwell's thesis (17), it was noticed that the selection of the endosteal chord lengths was performed by assuming a random entry and exit angle in the endosteum region. Because Whitwell was trying to derive an average chord length distribution in the 10- μm layer of endosteum, a random direction of entry and exit should have been used. In other words, because Whitwell was simulating the randomness of the entry and exit directions of the particle within the endosteum region, the solid angle should have been randomly selected and not simply the polar angle. The average chord lengths through the endosteum as determined in the present model and as assumed by Whitwell are presented in Table 5. As expected, our calculated average chord lengths are systematically larger than those of Whitwell, leading to larger calculated absorbed fractions for an endosteal target region.

Bone Trabeculae as Radiation Target

The last radiation target to be considered is the TBV. Although this target is not of importance for radiation protection, there is some interest in considering it as a radiation target for the alleviation of bone pain using radionuclide therapy (1,37). Three graphs are presented in Figure 11, each corresponding to one of three possible trabecular bone sources: the TMS, the TBE and the TBV. Variations observed in the absorbed fractions with initial electron energy are complementary but inverted to those observed when the TMS was considered the target region (Fig. 8). The highest absorbed fraction of energy is for the parietal bone because it represents the skeletal site with the largest bone trabeculae and the smallest marrow cavities.

As seen for the previous trabecular targets, the absorbed fraction to the TBV at high electron initial energies is

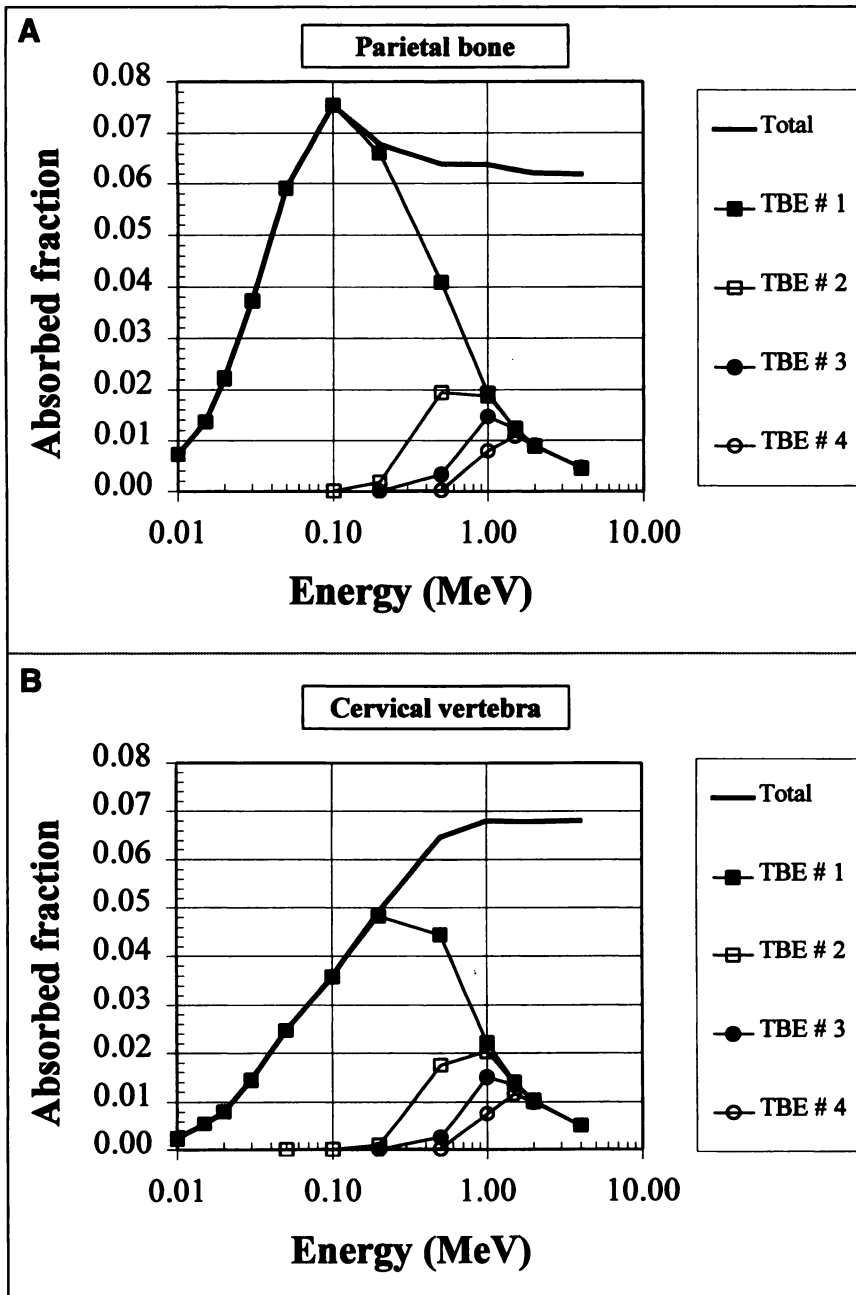


FIGURE 10. Absorbed fraction for trabecular bone endosteum (TBE) as target and TMS as source for parietal bone (A) and cervical vertebra (B). Total absorbed fraction to TBE is partitioned as function of number of trabecular bone endosteal layers separating TMS source and TBE target considered (i.e., TBE 1 is TBE directly adjacent to marrow space source).

independent of the source considered. This limit corresponds to the fractional track length in the bone trabeculae for the given bone site:

$$\phi(\text{TBV} \leftarrow \text{S}) = \frac{\langle d_{\text{T}} \rangle_{\mu}}{\langle d_{\text{MC}} \rangle_{\mu} + \alpha \langle d_{\text{T}} \rangle_{\mu}}, \quad \text{Eq. 13}$$

where $\langle d_{\text{MC}} \rangle_{\mu}$, $\langle d_{\text{T}} \rangle_{\mu}$ and α were defined previously. These limits of the absorbed fraction at large energy for each trabecular bone sites are verified in Table 4.

Comparisons with One-Dimensional Electron Transport Model

A one-dimensional model of electron transport in trabecular bone was also constructed to verify and compare

absorbed fraction results from the three-dimensional model presented. Following the methodology used in the three-dimensional model, chord lengths were sampled in all three regions of the trabecular bone to construct the one-dimensional geometry presented to the electron. The energy deposited in a given region was scored, assuming a straight trajectory of the electron through each tissue region and using the range-energy relationship methodology adopted by Whitwell (17) and Whitwell and Spiers (18) and by Eckerman (26). The range-energy relationship used was:

$$R = AE^m, \quad \text{Eq. 14}$$

where the values of m and A used in this research were derived using curve fits to the soft-tissue composition data

TABLE 5

Comparison of Mean Chord Lengths Through Endosteum as Reported by Whitwell and Calculated in Present Model of Electron Transport in Trabecular Bone

Bone site	Mean endosteum chord length (μm)	
	Whitwell* random angle	Present model random direction
Parietal bone	35	40
Cervical vertebra	39	49
Lumbar vertebra	41	51
Rib	43	54
Iliac crest	39	50
Femur head	41	52
Femur neck	43	55

*Data extracted from Whitwell (17).

given in ICRU Report 37 (38). Table 6 gives calculated values of A and m. These values are given such that if E is in MeV, R will be in units of g/cm². The error on the curve fitting is <1% at all energies. For the bone tissue, the ratio of the range (cm) in tissue to that in bone is approximately a constant over the energy-range of interest (1 keV to 5 MeV) and is equal to 1.7. Therefore, the energy-range relationship for bone was derived from that predicted in soft tissue using Equation 14.

Using this technique, absorbed fractions of energy were calculated for the same combinations of bone site, electron energy, source region and target region considered in the three-dimensional transport model. A total of 100,000 particles was sampled per bone site for each source region and electron initial energy.

Figure 12 gives the comparison between the absorbed fractions of energy calculated using the three-dimensional and one-dimensional transport models. In Figure 12, the ratio of absorbed fractions from the three-dimensional and one-dimensional models, averaged over all seven bone sites, is plotted as a function of the initial electron energy. Various source and target combinations are considered. Globally, good agreement is seen between the two calculations. Differences are larger at low energies, up to ~80%, but these discrepancies decrease as the electron initial energy increases (the maximum error at 4 MeV is 6%). This data agreement was not unexpected because the same chord length distributions were taken as input to both models.

If one considers the absorbed fractions of energy calculated when the source and the target regions are identical (Fig. 12), there is a very good agreement, except when the source-target region is the TBE. In this case, the difference is first very small and then increases to a maximum of 14% at 200 keV. Results from the two models converge again at higher energies. These differences are attributed to differ-

ences in the physics of the transport: a three-dimensional Monte Carlo transport code with angular straggling and production and transport of secondary electrons versus a one-dimensional continuous slowing-down approximation

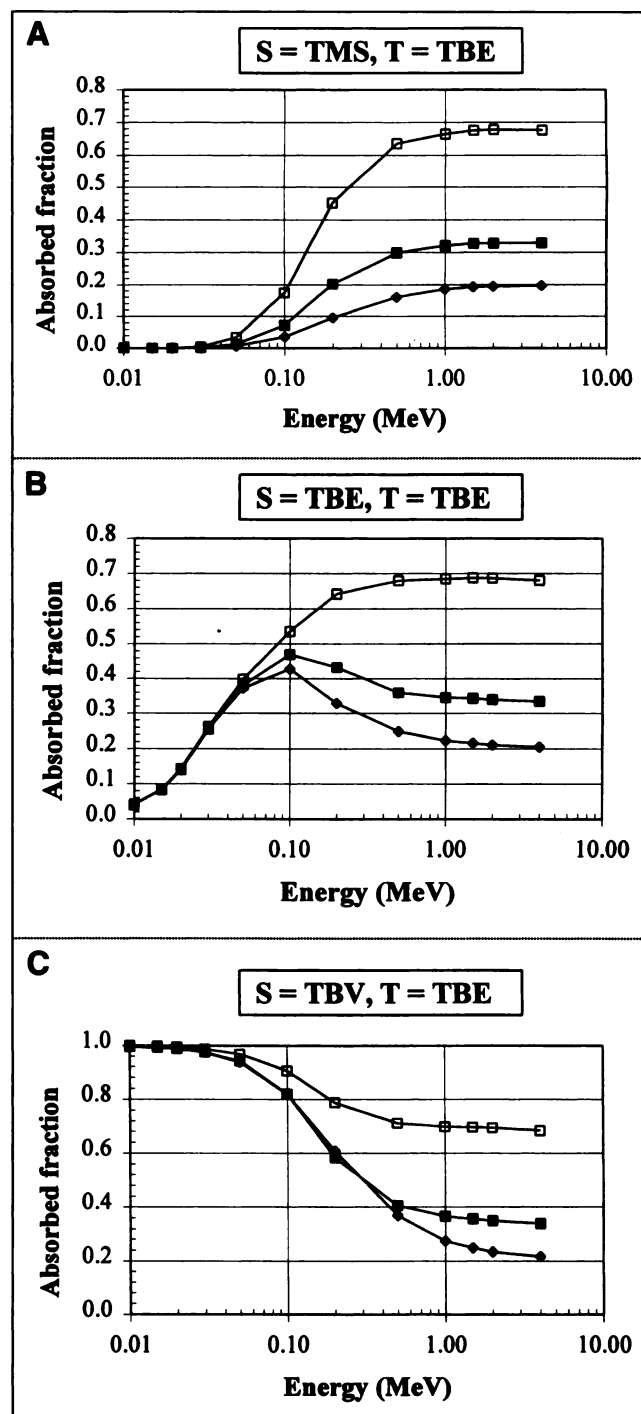


FIGURE 11. Absorbed fraction of energy to trabecular bone volume (TBV) for monoenergetic electrons for sources in trabecular marrow space (TMS) (A), trabecular bone endosteum (TBE) (B) and TBV (C). Three trabecular bone sites are shown: cervical vertebra (■), parietal bone (□) and rib (◆). S = source; T = target.

TABLE 6
Coefficients Used to Calculate CSDA Ranges for Electrons
in a Soft-Tissue Medium*

Energy range (MeV)	$R_{\text{CSDA}}(\text{g/cm}^2) = A \times E^m$	
	A	m
0.00 < E ≤ 0.05	0.86341	1.7682
0.05 < E ≤ 0.10	0.76684	1.7285
0.10 < E ≤ 0.30	0.59607	1.6138
0.30 < E ≤ 0.60	0.47275	1.4270
0.60 < E ≤ 2.00	0.43234	1.1990
2.00 < E ≤ 5.00	0.49150	1.0233

*Derived from data in International Commission on Radiological Units Report 37 (38). Error on interpolation in all cases is <1%.
CSDA = continuous slowing-down approximation.

(CSDA) calculation using a range-energy relationship for electrons.

The largest differences between models are seen when the source and the target are not adjacent regions, i.e., when the TMS and TBV are considered the source or target regions (Fig. 12). In this case, we see differences 30%–50% and upward for energies <100 keV. Because of the possible variations in the range of electrons modeled by the EGS4 Monte Carlo transport code (i.e., range straggling), we see low-energy electrons reaching these nonadjacent regions using the three-dimensional model, but they do not in the one-dimensional model. Differences of ~10% are also seen for energies <100 keV when the source is the TBE and the target is the TMS or TBV (Fig. 12). Finally, when one considers the TBE as a target, and the TMS and TBV as source regions (Fig. 12), good agreement is seen between the two transport methodologies at all electron energies.

Comparisons with Previously Published Electron Absorbed Fractions

It is also of interest to compare absorbed fraction results with the model of electron transport in trabecular bone used in the MIRDOSE3 program (25,26). In Eckerman (26), absorbed fractions are given only for the parietal bone and the lumbar vertebra, for the trabecular bone and red marrow as source regions and for the bone surface and red marrow as target regions. Because this model is a one-dimensional transport model, we compared absorbed fraction results with the one-dimensional transport model developed in this article. Table 7 gives ratios of absorbed fractions of energy for the lumbar vertebra and parietal bone and for several source and target region combinations. Eckerman's (26) red marrow, bone surface and trabecular bone regions are associated with our definitions of the TMS, TBE and TBV, respectively.

When the TMS is considered both the source and the target region, good agreement is seen for energies <100 keV. For higher electron energies this difference becomes ~5% for the lumbar vertebra and ~13% for the parietal bone. This difference can be analyzed if we consider the trabecular marrow cavity (TMC = TMS + TBE) as the chosen target region instead of the TMS. In this case, ratios between the two absorbed fractions are very close to unity. Consequently, it seems that the Eckerman (26) electron transport model does not distinguish between the marrow cavity and the marrow space. This can also be verified with the TBV as the source region and the TMS and TMC as the target regions. This comparison clearly indicates that the full marrow cavity, as given by the Spiers chord distribution (17), was considered when estimating red marrow absorbed fractions in the model of Eckerman (26).

One can also look at differences between these two one-dimensional electron transport models when the TBE is

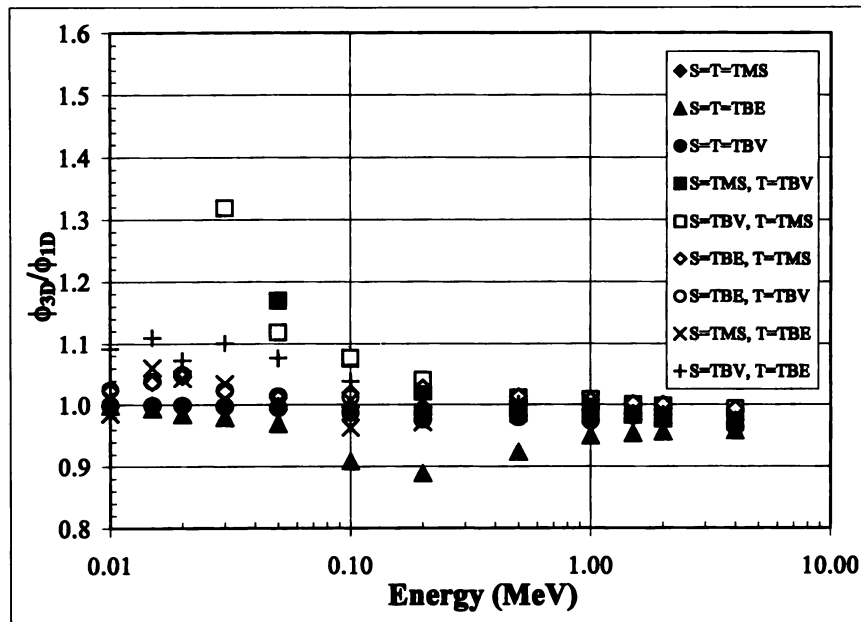


FIGURE 12. Ratios of absorbed fractions calculated using three-dimensional (3D) transport model of electron transport in trabecular bone and one-dimensional model (1D), as a function of electron initial kinetic energy. Ratios represent averages across all seven bone sites for each source (S)-target (T) combination. Individual differences at a specific bone site can therefore exceed these values. TMS = trabecular marrow space; TBE = trabecular bone endosteum; TBV = trabecular bone volume.

TABLE 7
Ratios of Absorbed Fraction of Energy in Trabecular Bone Calculated Using One-Dimensional Transport Model of This Study and of Eckerman

Lumbar vertebra*						
Energy (MeV)	$\frac{\phi(\text{TMS} \leftarrow \text{TMS})}{\phi(\text{RM} \leftarrow \text{RM})}$	$\frac{\phi(\text{TMS} \leftarrow \text{TBV})}{\phi(\text{RM} \leftarrow \text{TB})}$	$\frac{\phi(\text{TMC} \leftarrow \text{TMS})}{\phi(\text{RM} \leftarrow \text{RM})}$	$\frac{\phi(\text{TMC} \leftarrow \text{TBV})}{\phi(\text{RM} \leftarrow \text{TB})}$	$\frac{\phi(\text{TBE} \leftarrow \text{TMS})}{\phi(\text{BS} \leftarrow \text{RM})}$	$\frac{\phi(\text{TBE} \leftarrow \text{TBV})}{\phi(\text{BS} \leftarrow \text{TB})}$
Column no.†	1	2	3	4	5	6
0.010	1.00	0.00	1.01	0.94	0.07	0.94
0.030	0.99	0.05	1.03	1.02	0.48	1.04
0.050	0.98	0.30	1.05	1.05	0.92	1.19
0.100	0.96	0.59	1.06	1.01	1.55	1.56
0.500	0.84	0.81	1.02	1.03	1.83	2.06
2.000	0.81	0.81	1.01	1.02	1.99	2.02
4.000	0.82	0.81	1.02	1.02	2.01	2.03

Parietal bone*						
Energy (MeV)	$\frac{\phi(\text{TMS} \leftarrow \text{TMS})}{\phi(\text{RM} \leftarrow \text{RM})}$	$\frac{\phi(\text{TMS} \leftarrow \text{TBV})}{\phi(\text{RM} \leftarrow \text{TB})}$	$\frac{\phi(\text{TMC} \leftarrow \text{TMS})}{\phi(\text{RM} \leftarrow \text{RM})}$	$\frac{\phi(\text{TMC} \leftarrow \text{TBV})}{\phi(\text{RM} \leftarrow \text{TB})}$	$\frac{\phi(\text{TBE} \leftarrow \text{TMS})}{\phi(\text{BS} \leftarrow \text{RM})}$	$\frac{\phi(\text{TBE} \leftarrow \text{TBV})}{\phi(\text{BS} \leftarrow \text{TB})}$
Column no.†	1	2	3	4	5	6
0.010	1.00	0.00	1.00	0.95	0.05	1.27
0.030	1.00	0.05	1.01	1.01	0.35	1.19
0.050	1.00	0.31	1.01	1.00	0.65	1.30
0.100	0.99	0.67	1.02	1.05	1.07	1.64
0.500	0.94	0.91	1.01	1.02	1.96	2.03
2.000	0.93	0.92	1.01	1.01	2.06	1.93
4.000	0.93	0.92	1.01	1.01	2.13	1.94

*Notation for source and target regions reflects model used for calculation of absorbed fraction. In Eckerman (26), RM = red marrow; BS = bone surface; TB = trabeculae; TMC = trabecular marrow cavity (i.e., TMS + TBE).

†For easy readability with associated text, column numbers are assigned.

TMS = trabecular marrow space; TBV = trabecular bone volume; TBE = trabecular bone endosteum.

considered the target region. For both TMS and TBV electron sources, large differences are seen between the two models. Eckerman (26) provides few details as to how the endosteum is treated as a target region. Consequently, it is not possible to fully explain these differences.

Consideration of Trabecular Active Marrow as Target Region

When the Spiers (17) chord length distributions are used to construct a radiation transport model of the trabecular bone, the only source and target regions that can be considered are the TMS, TBE and TBV. However, it is of interest to derive absorbed fractions of energy to the trabecular active marrow (TAM) because this tissue is generally the radiosensitive target of interest. Because the TAM is contained within the TMS, one could assume that for a given source region, the electron energy is uniformly deposited across the TMS. Under this assumption, it is possible to calculate the absorbed fraction to the TAM for bone site j using the volume fraction of active marrow within the TMS:

$$\phi_j(\text{TAM} \leftarrow \text{S}) = \frac{V_{\text{TAM},j}}{V_{\text{TMS},j}} \phi_j(\text{TMS} \leftarrow \text{S}), \quad \text{Eq. 15}$$

where $V_{\text{TAM},j}$ and $V_{\text{TMS},j}$ represent the volume occupied by the TAM and TMS, respectively, within bone site j. Because the densities of the marrow space and red marrow are essentially equal, one can simplify Equation 15 using the definition of the CF given in Equation 7:

$$\phi_j(\text{TAM} \leftarrow \text{S}) = \text{CF}_j \phi_j(\text{TMS} \leftarrow \text{S}). \quad \text{Eq. 16}$$

It is important to note that this equation is valid only in the case of a source located within the TMS, TBE or TBV. It is currently not possible to calculate the absorbed fractions of energy for a source located in the TAM because the location of the TAM within the TMS is not known. For trabecular marrow sources, it is thus advisable to use the TMS as the source region until such time as more definitive histologic information permits the construction of models with true active marrow source regions.

CONCLUSION

A new model of electron transport in trabecular bone is presented in which the chord length distributions measured by Beddoe (7), Beddoe et al. (8) and Darley (9) are used to create a

three-dimensional transport model for use with the EGS4/PRESTA electron code (10-12). The model represents a logical three-dimensional extension of currently used one-dimensional transport models so that electron backscatter, delta rays and bremsstrahlung photons are explicitly considered during particle transport. Results of the transport calculations were expressed subsequently as absorbed fractions of energy for seven trabecular

bone sites, 12 electron energies and all source-target regions of interest (TMS, TBE and TBV). As with the skeletal model of MIRDOSE3, values of absorbed fraction given here represent a substantial improvement over the relatively energy-independent values of ICRP Publication 30 (24). Significant differences are noted in the absorbed fraction results from both three-dimensional and one-dimensional models for TMS-TBV source-

APPENDIX

TABLE 1A

Absorbed Fractions of Energy for Monoenergetic Electrons Emitted Within Trabecular Marrow Space

Target = Trabecular marrow space							
Energy (MeV)	Cervical vertebra	Femur head	Femur neck	Iliac crest	Lumbar vertebra	Parietal bone	Rib
0.010	9.98E-01	9.98E-01	9.99E-01	9.97E-01	9.98E-01	9.93E-01	9.99E-01
0.015	9.95E-01	9.96E-01	9.98E-01	9.95E-01	9.96E-01	9.86E-01	9.98E-01
0.020	9.92E-01	9.94E-01	9.96E-01	9.92E-01	9.94E-01	9.78E-01	9.96E-01
0.030	9.84E-01	9.87E-01	9.92E-01	9.84E-01	9.88E-01	9.59E-01	9.92E-01
0.050	9.62E-01	9.72E-01	9.80E-01	9.62E-01	9.73E-01	9.07E-01	9.81E-01
0.100	8.92E-01	9.12E-01	9.40E-01	8.88E-01	9.20E-01	7.50E-01	9.44E-01
0.200	7.48E-01	7.91E-01	8.54E-01	7.36E-01	8.22E-01	4.80E-01	8.74E-01
0.500	6.36E-01	7.11E-01	7.54E-01	6.44E-01	7.35E-01	3.00E-01	7.97E-01
1.000	6.09E-01	6.93E-01	7.26E-01	6.26E-01	7.08E-01	2.69E-01	7.66E-01
1.500	6.01E-01	6.88E-01	7.18E-01	6.20E-01	7.00E-01	2.57E-01	7.56E-01
2.000	5.98E-01	6.85E-01	7.15E-01	6.17E-01	6.97E-01	2.53E-01	7.53E-01
4.000	5.89E-01	6.76E-01	7.05E-01	6.09E-01	6.87E-01	2.46E-01	7.42E-01

Target = Trabecular bone endosteum							
Energy (MeV)	Cervical vertebra	Femur head	Femur neck	Iliac crest	Lumbar vertebra	Parietal bone	Rib
0.010	2.31E-03	1.85E-03	1.35E-03	2.64E-03	1.93E-03	7.23E-03	1.04E-03
0.015	5.44E-03	3.62E-03	2.50E-03	4.78E-03	3.59E-03	1.36E-02	2.47E-03
0.020	7.99E-03	6.08E-03	4.17E-03	8.24E-03	6.02E-03	2.22E-02	4.13E-03
0.030	1.44E-02	1.20E-02	7.58E-03	1.51E-02	1.08E-02	3.73E-02	7.67E-03
0.050	2.47E-02	1.89E-02	1.33E-02	2.53E-02	1.79E-02	5.91E-02	1.28E-02
0.100	3.59E-02	2.98E-02	2.08E-02	3.87E-02	2.71E-02	7.55E-02	1.95E-02
0.200	4.91E-02	4.40E-02	2.98E-02	5.54E-02	4.08E-02	6.80E-02	3.04E-02
0.500	6.47E-02	6.15E-02	4.36E-02	7.18E-02	5.50E-02	6.39E-02	4.24E-02
1.000	6.80E-02	6.49E-02	4.71E-02	7.38E-02	5.87E-02	6.38E-02	4.61E-02
1.500	6.79E-02	6.53E-02	4.82E-02	7.42E-02	5.89E-02	6.27E-02	4.68E-02
2.000	6.78E-02	6.55E-02	4.81E-02	7.41E-02	5.94E-02	6.21E-02	4.70E-02
4.000	6.81E-02	6.56E-02	4.83E-02	7.41E-02	5.95E-02	6.18E-02	4.75E-02

Target = Trabecular bone volume							
Energy (MeV)	Cervical vertebra	Femur head	Femur neck	Iliac crest	Lumbar vertebra	Parietal bone	Rib
0.010	2.18E-05	0.00E+00	5.15E-06	4.10E-06	4.77E-06	3.15E-05	0.00E+00
0.015	8.80E-06	1.13E-05	0.00E+00	3.80E-05	2.33E-05	6.85E-05	5.57E-06
0.020	6.33E-05	1.79E-05	2.36E-05	5.60E-05	2.01E-05	2.70E-04	1.81E-05
0.030	1.24E-03	9.81E-04	7.56E-04	1.35E-03	8.66E-04	3.88E-03	6.46E-04
0.050	1.29E-02	9.48E-03	6.66E-03	1.30E-02	9.55E-03	3.44E-02	6.57E-03
0.100	7.23E-02	5.82E-02	3.94E-02	7.36E-02	5.25E-02	1.74E-01	3.62E-02
0.200	2.02E-01	1.64E-01	1.16E-01	2.08E-01	1.37E-01	4.52E-01	9.51E-02
0.500	2.98E-01	2.26E-01	2.01E-01	2.84E-01	2.09E-01	6.35E-01	1.60E-01
1.000	3.20E-01	2.39E-01	2.24E-01	2.97E-01	2.31E-01	6.64E-01	1.85E-01
1.500	3.26E-01	2.42E-01	2.29E-01	3.00E-01	2.36E-01	6.75E-01	1.92E-01
2.000	3.27E-01	2.43E-01	2.31E-01	3.02E-01	2.37E-01	6.77E-01	1.94E-01
4.000	3.28E-01	2.44E-01	2.33E-01	3.02E-01	2.39E-01	6.75E-01	1.96E-01

target combinations at low electron energies (<100 keV). Results for endosteum self-irradiation show skeletal-averaged differences up to 14% between one-dimensional and three-dimensional transport at electron energies of a few hundred keV. Direct comparisons with the underlying model of MIRDOSE3 indicate that marrow dose estimates are treated to the exclusion of endosteum dose estimates, for which specific details are not given.

The model represents a three-dimensional transport model

of electrons in trabecular bone and is not to be interpreted as a geometric model of the trabecular microstructure. Future improvements in bone dosimetry models await more realistic characterizations of trabecular bone microarchitecture as suggested by Jokisch et al. (39) using direct imaging techniques such as MR microscopy. It is anticipated that these techniques will permit an expansion of Reference Man skeletal models to more explicitly account for variations in trabecular microstructure.

TABLE 2A
Absorbed Fractions of Energy for Monoenergetic Electrons Emitted Within Trabecular Bone Endosteum

Target = Trabecular marrow space							
Energy (MeV)	Cervical vertebra	Femur head	Femur neck	Iliac crest	Lumbar vertebra	Parietal bone	Rib
0.010	3.63E-02	3.76E-02	3.80E-02	3.71E-02	3.59E-02	3.29E-02	3.77E-02
0.015	7.47E-02	7.86E-02	7.76E-02	7.57E-02	7.72E-02	6.82E-02	7.69E-02
0.020	1.26E-01	1.31E-01	1.31E-01	1.28E-01	1.27E-01	1.13E-01	1.29E-01
0.030	2.28E-01	2.37E-01	2.37E-01	2.35E-01	2.34E-01	2.06E-01	2.34E-01
0.050	3.29E-01	3.47E-01	3.45E-01	3.39E-01	3.37E-01	2.90E-01	3.40E-01
0.100	3.99E-01	4.22E-01	4.33E-01	4.22E-01	4.17E-01	3.23E-01	4.37E-01
0.200	4.76E-01	5.50E-01	5.34E-01	5.22E-01	5.47E-01	2.74E-01	5.82E-01
0.500	5.64E-01	6.45E-01	6.60E-01	5.98E-01	6.44E-01	2.50E-01	6.87E-01
1.000	5.79E-01	6.64E-01	6.84E-01	6.07E-01	6.67E-01	2.46E-01	7.18E-01
1.500	5.80E-01	6.68E-01	6.92E-01	6.07E-01	6.75E-01	2.43E-01	7.27E-01
2.000	5.83E-01	6.70E-01	6.96E-01	6.08E-01	6.77E-01	2.42E-01	7.31E-01
4.000	5.81E-01	6.69E-01	6.95E-01	6.05E-01	6.78E-01	2.40E-01	7.31E-01
Target = Trabecular bone endosteum							
Energy (MeV)	Cervical vertebra	Femur head	Femur neck	Iliac crest	Lumbar vertebra	Parietal bone	Rib
0.010	9.23E-01	9.22E-01	9.22E-01	9.22E-01	9.25E-01	9.27E-01	9.22E-01
0.015	8.43E-01	8.40E-01	8.39E-01	8.43E-01	8.39E-01	8.47E-01	8.40E-01
0.020	7.36E-01	7.29E-01	7.29E-01	7.33E-01	7.34E-01	7.45E-01	7.33E-01
0.030	5.17E-01	5.08E-01	5.09E-01	5.10E-01	5.12E-01	5.33E-01	5.11E-01
0.050	2.90E-01	2.80E-01	2.83E-01	2.88E-01	2.87E-01	3.12E-01	2.88E-01
0.100	1.31E-01	1.24E-01	1.25E-01	1.31E-01	1.35E-01	1.43E-01	1.36E-01
0.200	9.13E-02	9.31E-02	7.85E-02	9.40E-02	9.57E-02	8.33E-02	8.95E-02
0.500	7.58E-02	7.51E-02	5.84E-02	8.02E-02	7.21E-02	6.88E-02	6.20E-02
1.000	7.26E-02	7.08E-02	5.39E-02	7.80E-02	6.62E-02	6.57E-02	5.53E-02
1.500	7.12E-02	6.87E-02	5.14E-02	7.66E-02	6.38E-02	6.39E-02	5.18E-02
2.000	7.02E-02	6.83E-02	5.07E-02	7.57E-02	6.29E-02	6.31E-02	5.11E-02
4.000	6.92E-02	6.73E-02	4.96E-02	7.52E-02	6.13E-02	6.25E-02	4.94E-02
Target = Trabecular bone volume							
Energy (MeV)	Cervical vertebra	Femur head	Femur neck	Iliac crest	Lumbar vertebra	Parietal bone	Rib
0.010	4.04E-02	4.06E-02	3.97E-02	4.05E-02	3.95E-02	4.00E-02	4.08E-02
0.015	8.23E-02	8.17E-02	8.35E-02	8.12E-02	8.37E-02	8.44E-02	8.33E-02
0.020	1.39E-01	1.41E-01	1.40E-01	1.39E-01	1.39E-01	1.43E-01	1.38E-01
0.030	2.55E-01	2.55E-01	2.54E-01	2.56E-01	2.54E-01	2.61E-01	2.55E-01
0.050	3.81E-01	3.73E-01	3.73E-01	3.73E-01	3.76E-01	3.98E-01	3.72E-01
0.100	4.69E-01	4.54E-01	4.41E-01	4.47E-01	4.49E-01	5.35E-01	4.27E-01
0.200	4.32E-01	3.57E-01	3.87E-01	3.84E-01	3.57E-01	6.42E-01	3.28E-01
0.500	3.59E-01	2.79E-01	2.80E-01	3.21E-01	2.82E-01	6.80E-01	2.49E-01
1.000	3.46E-01	2.62E-01	2.59E-01	3.12E-01	2.64E-01	6.85E-01	2.24E-01
1.500	3.43E-01	2.58E-01	2.51E-01	3.11E-01	2.56E-01	6.88E-01	2.16E-01
2.000	3.40E-01	2.55E-01	2.47E-01	3.09E-01	2.53E-01	6.87E-01	2.11E-01
4.000	3.34E-01	2.50E-01	2.40E-01	3.05E-01	2.47E-01	6.80E-01	2.05E-01

TABLE 3A
Absorbed Fractions of Energy for Monoenergetic Electrons Emitted Within Trabecular Bone Volume

Target = Trabecular marrow space							
Energy (MeV)	Cervical vertebra	Femur head	Femur neck	Iliac crest	Lumbar vertebra	Parietal bone	Rib
0.010	2.86E-06	0.00E+00	1.46E-05	0.00E+00	0.00E+00	0.00E+00	0.00E+00
0.015	2.01E-05	1.25E-05	7.35E-06	5.10E-06	2.27E-05	0.00E+00	2.26E-05
0.020	3.01E-05	2.19E-05	1.75E-05	2.56E-05	3.16E-05	0.00E+00	7.39E-06
0.030	1.57E-03	1.91E-03	1.65E-03	1.76E-03	1.68E-03	6.26E-04	1.74E-03
0.050	1.88E-02	2.37E-02	1.76E-02	2.20E-02	2.18E-02	9.20E-03	2.05E-02
0.100	1.15E-01	1.47E-01	1.05E-01	1.36E-01	1.31E-01	5.69E-02	1.18E-01
0.200	3.38E-01	4.26E-01	3.22E-01	3.97E-01	3.65E-01	1.56E-01	3.29E-01
0.500	5.21E-01	6.06E-01	5.84E-01	5.62E-01	5.74E-01	2.26E-01	5.73E-01
1.000	5.60E-01	6.46E-01	6.53E-01	5.90E-01	6.37E-01	2.37E-01	6.71E-01
1.500	5.68E-01	6.56E-01	6.71E-01	5.96E-01	6.55E-01	2.36E-01	6.97E-01
2.000	5.74E-01	6.62E-01	6.80E-01	6.00E-01	6.63E-01	2.37E-01	7.10E-01
4.000	5.77E-01	6.65E-01	6.87E-01	6.01E-01	6.71E-01	2.38E-01	7.21E-01

Target = Trabecular bone endosteum							
Energy (MeV)	Cervical vertebra	Femur head	Femur neck	Iliac crest	Lumbar vertebra	Parietal bone	Rib
0.010	3.71E-03	4.64E-03	3.14E-03	4.31E-03	4.34E-03	1.82E-03	4.04E-03
0.015	7.66E-03	9.25E-03	7.05E-03	9.00E-03	9.21E-03	3.94E-03	8.27E-03
0.020	1.27E-02	1.52E-02	1.11E-02	1.42E-02	1.43E-02	6.43E-03	1.28E-02
0.030	2.39E-02	2.78E-02	2.15E-02	2.76E-02	2.75E-02	1.30E-02	2.49E-02
0.050	4.10E-02	4.92E-02	3.68E-02	4.68E-02	4.69E-02	2.37E-02	4.35E-02
0.100	6.53E-02	7.94E-02	5.59E-02	7.44E-02	7.26E-02	3.87E-02	6.34E-02
0.200	7.84E-02	8.40E-02	6.37E-02	8.40E-02	7.59E-02	5.53E-02	6.29E-02
0.500	7.30E-02	7.31E-02	5.54E-02	7.73E-02	6.74E-02	6.15E-02	5.69E-02
1.000	7.08E-02	6.94E-02	5.19E-02	7.62E-02	6.44E-02	6.26E-02	5.25E-02
1.500	7.01E-02	6.85E-02	5.07E-02	7.57E-02	6.24E-02	6.19E-02	5.08E-02
2.000	6.97E-02	6.77E-02	5.04E-02	7.55E-02	6.17E-02	6.18E-02	4.98E-02
4.000	6.88E-02	6.69E-02	4.93E-02	7.47E-02	6.05E-02	6.15E-02	4.87E-02

Target = Trabecular bone volume							
Energy (MeV)	Cervical vertebra	Femur head	Femur neck	Iliac crest	Lumbar vertebra	Parietal bone	Rib
0.010	9.96E-01	9.95E-01	9.97E-01	9.96E-01	9.96E-01	9.98E-01	9.96E-01
0.015	9.92E-01	9.91E-01	9.93E-01	9.91E-01	9.91E-01	9.96E-01	9.92E-01
0.020	9.87E-01	9.85E-01	9.89E-01	9.86E-01	9.86E-01	9.94E-01	9.87E-01
0.030	9.75E-01	9.70E-01	9.77E-01	9.71E-01	9.71E-01	9.86E-01	9.73E-01
0.050	9.40E-01	9.27E-01	9.46E-01	9.31E-01	9.31E-01	9.67E-01	9.36E-01
0.100	8.20E-01	7.73E-01	8.39E-01	7.90E-01	7.97E-01	9.04E-01	8.18E-01
0.200	5.84E-01	4.89E-01	6.13E-01	5.19E-01	5.59E-01	7.88E-01	6.07E-01
0.500	4.05E-01	3.20E-01	3.60E-01	3.59E-01	3.57E-01	7.11E-01	3.68E-01
1.000	3.66E-01	2.82E-01	2.92E-01	3.30E-01	2.95E-01	6.98E-01	2.73E-01
1.500	3.56E-01	2.70E-01	2.73E-01	3.23E-01	2.77E-01	6.96E-01	2.48E-01
2.000	3.49E-01	2.63E-01	2.63E-01	3.18E-01	2.68E-01	6.93E-01	2.34E-01
4.000	3.39E-01	2.54E-01	2.49E-01	3.09E-01	2.54E-01	6.83E-01	2.16E-01

ACKNOWLEDGMENTS

This work was supported in part by U.S. Department of Energy Grant DE-FG05-95ER62006 and by the Health Physics Faculty Research Award Program Administered by Oak Ridge Associated Universities, Oak Ridge, TN. The research of Derek W. Jokisch was performed under appointment to the Nuclear Engineering/Health Physics Fellowship Program administered by Oak Ridge Institute for Science and Education for the U.S. Department of Energy. Lionel G. Bouchet is the

recipient of the Burton J. Moyer Memorial Health Physics Fellowship.

REFERENCES

- Lewington VJ. Cancer therapy using bone-seeking isotopes. *Phys Med Biol.* 1996;41:2027-2042.
- Siegel JA, Wessels BW, Watson EE. Bone marrow dosimetry and toxicity for radioimmunotherapy. *Antibody Immunoconjugates Radiopharm.* 1990;3:213-233.
- Sgouros G. Bone marrow dosimetry for radioimmunotherapy: theoretical considerations. *J Nucl Med.* 1993;34:689-694.

4. International Commission on Radiological Protection. *A Review of the Radiosensitivity of the Tissues in bone*. ICRP report 11. Oxford, UK: Pergamon; 1968.
5. International Commission on Radiological Protection. *Basic Anatomical and Physiological Data for Use in Radiological Protection: The Skeleton*. ICRP publication 70. Tarrytown, NY: Elsevier Science; 1995.
6. Bouchet LG, Bolch WE. A three-dimensional transport model for determining absorbed fractions of energy for electrons within cortical bone. *J Nucl Med*. 1999; in press.
7. Beddoe AH. *The Microstructure of Mammalian Bone in Relation to the Dosimetry of Bone-Seeking Radionuclides* [thesis]. Leeds, UK: University of Leeds; 1976.
8. Beddoe AH, Darley PJ, Spiers FW. Measurements of trabecular bone structure in man. *Phys Med Biol*. 1976;21:589-607.
9. Darley PJ. *An Investigation of the Structure of Trabecular Bone in Relation to the Radiation Dosimetry of Bone-Seeking Radionuclides* [thesis]. Leeds, UK: University of Leeds; 1972.
10. Bielajew AF, Rogers DWO. PRESTA, the "parameter reduced electron step transport algorithm" for electron Monte Carlo transport. *Nucl Instr Meth*. 1987;B18:165-181.
11. Nelson WR, Hirayama RH, Roger DWO. *The EGS4 Code System*. SLAC report 265. Palo Alto, CA: Stanford Linear Accelerator Center; 1985.
12. Ford RL, Nelson WR. *The EGS Code System: Computer Programs for Monte Carlo Simulation of Electromagnetic Cascade Shower*. SLAC report 210. Palo Alto, CA: Stanford Linear Accelerator Center; 1978.
13. Spiers FW. The influence of energy absorption and electron range on dosage in irradiated bone. *Br J of Radiol*. 1949;22:521-533.
14. Spiers FW, Beddoe AH, Whitwell JR. Mean skeletal dose factors for beta-particle emitters in human bone. Part II: surface-seeking radionuclides. *Br J Radiol*. 1981;54:500-504.
15. Spiers FW, Beddoe AH, Whitwell JR. Mean skeletal dose factors for beta-particle emitters in human bone. Part I: volume-seeking radionuclides. *Br J Radiol*. 1978;51:622-627.
16. Spiers FW, Whitwell JR, Beddoe AH. Calculated dose factors for the radiosensitive tissues in bone irradiated by surface-deposited radionuclides. *Phys Med Biol*. 1978;23:481-494.
17. Whitwell JR. *Theoretical Investigations of Energy Loss by Ionizing Particles in Bone* [thesis]. Leeds, UK: University of Leeds; 1973.
18. Whitwell JR, Spiers FW. Calculated beta-ray dose factors for trabecular bone. *Phys Med Biol*. 1976;21:16-38.
19. Spiers FW. Dosimetry at interfaces with special reference to bone. In: *Proceedings of the Symposium on Microdosimetry*: EAEC Report EUR 3734. Vienna, Austria: European Atomic Energy Commission; 1968:473-508.
20. Snyder WS, Ford MR, Warner GG, Watson SB. *A Tabulation of Dose Equivalent Per Microcurie-Day for Source and Target Organs of an Adult for Various Radionuclides*. ORNL-5000. Oak Ridge, TN: Oak Ridge National Laboratory; 1974.
21. Snyder WS, Ford MR, Warner GG, Watson SB. "S," *Absorbed Dose per Unit Cumulated Activity for Selected Radionuclides and Organs*. MIRD Pamphlet 11. New York, NY: Society of Nuclear Medicine; 1975.
22. Howell RW, Wessels BW, Loevinger R, et al. The MIRD perspective 1999: Medical Internal Radiation Dose Committee. *J Nucl Med*. 1999;40:3S-10S.
23. Loevinger R, Budinger TF, Watson EE. *MIRD Primer for Absorbed Dose Calculations*. Rev ed. New York, NY: Society of Nuclear Medicine; 1991.
24. International Commission on Radiological Protection. *Limits for Intakes of Radionuclides by Workers*. Publication 30. Oxford, UK: Pergamon; 1979.
25. Stabin MG. MIRDOSE: personal computer software for internal dose assessment in nuclear medicine. *J Nucl Med*. 1996;37:538-546.
26. Eckerman KF. Aspects of the dosimetry of radionuclides within the skeleton with particular emphasis on the active marrow. In: *Proceedings of the Fourth International Radiopharmaceutical Dosimetry Symposium*. 1985.CONF-85113. Oak Ridge, TN: Oak Ridge Associated Universities; 1985:514-534.
27. Cristy M, Eckerman KF. *Specific Absorbed Fractions of Energy at Various Ages from Internal Photon Sources*. ORNL/TM-8381. Oak Ridge, TN: Oak Ridge National Laboratory; 1987.
28. Samarungta RC, Thomas SR, Hinnefeld JD, et al. A Monte Carlo simulation model for radiation dose to metastatic skeletal tumor from rhenium-186(Sn)-HEDP. *J Nucl Med*. 1995;36:336-50.
29. International Commission on Radiological Protection. *Report on the Task Group on Reference Man*. ICRP publication 23. Oxford, UK: Pergamon; 1975.
30. International Commission on Radiological Protection. *Recommendations of the International Commission on Radiological Protection*. ICRP publication 26. Oxford, UK: Pergamon; 1977.
31. Coleman R. Random paths through convex bodies. *J Appl Prob*. 1969;6:430-441.
32. Eckerman KF, Ryman JC, Taner AC, Kerr GD. Traversal of cells by radiation and absorbed fraction estimates for electrons and alpha particles. In: *Proceedings of the Fourth International Radiopharmaceutical Dosimetry Symposium*. 1985; CONF-851113. Oak Ridge, TN: Oak Ridge Associated Universities; 1985:67-81.
33. Kellerer AM. Considerations on the random traversal of convex bodies and solutions for general cylinders. *Radiat Res*. 1971;47:359-376.
34. Cristy M. Active bone marrow distribution as a function of age in humans. *Phys Med Biol*. 1981;26:389-400.
35. International Commission on Radiation Units and Measurements. *Photon, Electron, Proton and Neutron Interaction Data for Body Tissues*. ICRU report 46. Bethesda, MD: International Commission on Radiation Units and Measurements; 1992.
36. International Commission on Radiation Units and Measurements. *Tissue Substitutes in Radiation Dosimetry and Measurement*. ICRU report 44. Bethesda, MD: International Commission on Radiation Units and Measurements; 1989.
37. Bouchet LG, Bolch WE, Goddu SM, Howell RW, Rao DV. Consideration in the selection of radiopharmaceuticals for palliation of bone pain from metastatic osseous lesions. *J Nucl Med*. In press.
38. International Commission on Radiation Units and Measurements. *Stopping Powers for Electrons and Positrons*. ICRU report 37. Bethesda, MD: International Commission on Radiation Units and Measurements; 1984.
39. Jokisch DW, Patton PW, Inglis BA, et al. NMR microscopy of trabecular bone and its role in skeletal dosimetry. *Health Phys*. 1998;75:584-96.